

Contents lists available at ScienceDirect

# Journal of Rock Mechanics and Geotechnical Engineering

journal homepage: www.jrmge.cn



Full Length Article

# Hybrid deep learning and isogeometric analysis for bearing capacity assessment of sand over clay



Toan Nguyen-Minh <sup>a</sup>, Tram Bui-Ngoc <sup>b, c</sup>, Jim Shiau <sup>d</sup>, Tan Nguyen <sup>e, \*</sup>, Trung Nguyen-Thoi <sup>f, c</sup>

- <sup>a</sup> Faculty of Civil Engineering, Ton Duc Thang University, Ho Chi Minh City, 700000, Viet Nam
- b Laboratory for Computational Mechanics, Institute for Computational Science and Artificial Intelligence, Van Lang University, Ho Chi Minh City, 700000, Viet Nam
- <sup>c</sup> Faculty of Mechanical Electrical and Computer Engineering, School of Technology, Van Lang University, Ho Chi Minh City, 700000, Viet Nam
- <sup>d</sup> School of Engineering, University of Southern Queensland, Toowoomba, QLD, 4350, Australia
- e Smart Computing in Civil Engineering Research Group, Faculty of Civil Engineering, Ton Duc Thang University, Ho Chi Minh City, 700000, Viet Nam
- f Laboratory for Applied and Industrial Mathematics, Institute for Computational Science and Artificial Intelligence, Van Lang University, Ho Chi Minh City, 700000. Viet Nam

#### ARTICLE INFO

# Article history: Received 24 April 2024 Received in revised form 4 September 2024 Accepted 10 October 2024 Available online 24 November 2024

Keywords: UB limit analysis Isogeometric analysis (IGA) Hybrid deep neural network Whale optimization algorithm

#### ABSTRACT

In this paper, Isogeometric analysis (IGA) is effectively integrated with machine learning (ML) to investigate the bearing capacity of strip footings in layered soil profiles, with a focus on a sand-over-clay configuration. The study begins with the generation of a comprehensive dataset of 10,000 samples from IGA upper bound (UB) limit analyses, facilitating an in-depth examination of various material and geometric conditions. A hybrid deep neural network, specifically the Whale Optimization Algorithm-Deep Neural Network (WOA-DNN), is then employed to utilize these 10,000 outputs for precise bearing capacity predictions. Notably, the WOA-DNN model outperforms conventional ML techniques, offering a robust and accurate prediction tool. This innovative approach explores a broad range of design parameters, including sand layer depth, load-to-soil unit weight ratio, internal friction angle, cohesion, and footing roughness. A detailed analysis of the dataset reveals the significant influence of these parameters on bearing capacity, providing valuable insights for practical foundation design. This research demonstrates the usefulness of data-driven techniques in optimizing the design of shallow foundations within layered soil profiles, marking a significant stride in geotechnical engineering advancements.

© 2025 Institute of Rock and Soil Mechanics, Chinese Academy of Sciences. Published by Elsevier B.V. This is an open access article under the CC BY-NC-ND license (http://creativecommons.org/licenses/by-nc-nd/

4.0/).

# 1. Introduction

Determining the ultimate bearing capacity of shallow foundations on layered soil systems, particularly those involving sand overlying clay, presents an ongoing challenge in geotechnical engineering. The accuracy of these capacity assessments is of paramount importance for the safe and efficient design of foundations. However, existing theoretical approaches often fall short of providing precise estimations, highlighting the critical need to bridge the gap between theory and practical application (Shoaei et

E-mail address: nguyentan@tdtu.edu.vn (T. Nguyen).

#### al., 2012).

Meyerhof's pivotal work in 1974 provided a fundamental conceptual framework for understanding two common scenarios: loose sand over stiff clay and dense sand over soft clay (Meyerhof, 1974). In the case of loose sand over stiff clay, the bearing capacity predominantly relates to the top layer, and the failure surface remains confined within it. Conversely, when dense sand overlies a soft clay bed, the shear failure zone tends to extend into the bottom soft layer, thus creating the challenge of maintaining the continuity of the shear zone at the interface between the two layers.

Expanding on Meyerhof's insights, Hanna's research in 1982 made a notable contribution to the formulation of ultimate bearing capacity (Hanna, 1982). Hanna's modifications to Terzaghi's classical equation ensured that the results did not exceed the bearing capacity of the lower stiff layer. He introduced modified bearing

<sup>\*</sup> Corresponding author. Smart Computing in Civil Engineering Research Group, Faculty of Civil Engineering, Ton Duc Thang University, Ho Chi Minh City, 700000, Viet Nam.

capacity factors that considered density and overburden terms as functions of the foundation depth (H), width (B), and the internal angle of friction. Hanna's work in 1981 extended the analysis to cases where strong sand overlies a weaker clay layer (Hanna, 1981). In such scenarios, punching shear theory was applied, defining a failure zone resembling a truncated pyramid that penetrates the bottom layer. Specific equations were developed for situations involving strong sand over weak clay, offering a solution to enhance subsoil bearing capacity by replacing the top loose sand layer with a stronger alternative e.g. Meyerhof (1974), Hanna and Meyerhof (1980), Okamura et al. (1998), among others.

While Terzaghi's classical bearing capacity equation and dimensionless bearing capacity factors are sufficient for assessing bearing capacity in homogeneous soils, they do not universally apply to layered soil systems. As a result, extensive research has been dedicated to understanding the intricacies of bearing capacity in these complex scenarios. Numerous researchers, including Meyerhof (1974), Craig and Chua (1990), Okamura et al. (1997), Teh et al. (2008, 2010), and Lee et al. (2013a, b), have made substantial contributions to this ongoing quest. Their work combines both experimental testing and theoretical analysis to address the challenges posed by layered soil systems and provide more accurate estimations of bearing capacity.

In the realm of analytical methods, two semi-empirical methods, known as the load-spread method and the punchingshear method, have gained prominence for determining bearing capacity in layered soil systems where sand overlies clay. These methods, grounded in the concept of limit equilibrium, have demonstrated useful results with reasonable estimates on the conservative side. They were recommended for calculating ultimate bearing capacity in the new ISO standard 19905-1 (Wong et al., 2012). Additionally, Pham and Ohtsuka (2021) conducted a rigorous investigation into the bearing capacity of rigid footings on sand over clay using the rigid-plastic finite-element method (RPFEM). Their study highlighted the critical role of interface elements and frictional conditions in influencing failure mechanisms. Tang et al. (2017) contributed significantly by assessing model factors for bearing capacity calculations through an extensive analysis of centrifuge test data. Their findings shed light on the accuracy and applicability of traditional methods across varying soil densities.

Recent advancements in geotechnical engineering research have introduced analytical and computational methods to tackle the complexities of bearing capacity estimation. Analytical limit analysis methods, such as those by Michalowski and Shi (1995), along with finite element limit analysis (FELA) methods, have provided UB solutions that offer insights into failure mechanisms (Haghighi et al., 2019; Salimi Eshkevari et al., 2019; Shiau et al., 2003). FELA methods, in particular, have enabled the capture of intricate bearing capacity behaviors. Notably, Shiau et al. (2003) employed advanced upper and lower bound techniques to determine the ultimate bearing capacity of strip footings on sand over clay, ensuring a  $\pm 10\%$  accuracy in their results. Their study focused on limit analysis for layered soil-bearing capacity, emphasizing the application of finite elements. More recently, Salimi Eshkevari et al. (2019) presented improved bearing capacity for shallow foundations on layered soil profiles with a sand layer over clay using FELA. Rajaei et al. (2018) explored improvements in bearing capacity through variations in sand layer characteristics and surcharge pressures, underscoring the advantages of a layered substrate over homogeneous clay. Their work led to a simplified yet accurate bearing capacity model that considers shear resistance variations in the sand layer relative to the dimensionless undrained strength of the clay layer, proving to be a valuable tool for practical applications for working platform design. Their results of FELA analyses have

paved the way for the proposal of a comprehensive bearing capacity model that seeks to unify Terzaghi's and Meyerhof's solutions.

Nonetheless, there are limitations associated with traditional finite element method (FEM)-based FELA approaches. These limitations include constrained computational capabilities and modeling constraints, which can hinder the comprehensive analysis of bearing capacity in layered soil systems. To address these limitations, this study introduces an innovative approach that leverages IGA and upper-bound limit analysis. IGA provides a robust framework for modeling complex geometries and has demonstrated significant potential in enhancing limit analysis (Hughes et al., 2005; Nguyen and Tran, 2021; Nguyen-Minh et al., 2023). Additionally, this study incorporates Second-Order Cone Programming (SOCP) optimization, offering a versatile and powerful tool for upper-bound limit analysis (Makrodimopoulos and Martin, 2007, Nguyen et al., 2022; Nguyen and Nguyen-Son, 2022).

One notable aspect of this study is the utilization of extensive data comprising 10,000 input samples generated by the proposed IGA-UB model, covering a wide array of material and geometrical scenarios and conditions. This dataset significantly expands the existing knowledge base in the field by feeding robust ML models, which have recently emerged as a valuable tool in geotechnical engineering, particularly in predicting ultimate bearing capacity. Recent advancements in geotechnical engineering have demonstrated the efficacy of various ML methods, including decision trees, random forests, artificial neural networks, Bayesian learning, and genetic programming, in addressing complex geological conditions. Genetic programming, in particular, has shown promise due to its ability to generate explicit equations for geotechnical problems. Studies by Cheng et al. (2022, 2023a, b) have validated the feasibility and reliability of genetic programming in predicting fieldmonitored suction variations, approximating shield tunnelinginduced surface settlement, and analyzing rainfall-induced soil suction responses. These advancements highlight the potential of data-driven approaches in enhancing the accuracy and applicability of bearing capacity assessments in layered soil systems. Researchers have explored the application of Artificial Neural Networks (ANNs) and other ML models e.g., Moayedi and Rezaei (2020), Ebid et al. (2022), and Moayedi et al. (2019a, b). These models leverage data-driven insights to predict bearing capacity, offering a unique approach compared to classical and numerical methods. However, many of these studies have focused primarily on the strength of hybrid ML models, sometimes overlooking aspects related to physical interpretation and practical decisionmaking. Furthermore, the datasets used in these studies have often been limited in scope.

To fill these knowledge gaps, this paper presents a novel approach leveraging the extensive dataset produced by the -UB IGA model. This research introduces a hybrid Deep Feedforward Neural Network (DFNN) optimized using the WOA proposed by Mirjalili and Lewis (2016). DFNN, a fundamental model in deep learning (DL), is designed to hierarchically learn complicated data representations through multiple layers of transformation (Najafabadi et al., 2015; Goodfellow et al., 2016). The discretization method using IGA streamlines the generation of large datasets by automatically varying input parameters, thereby automating the process substantially. This capability not only enables the creation of extensive datasets, which would be prohibitively time-consuming to compile manually for each scenario, but also ensures their independence from subjective biases inherent in manual data collection. Such a rigorously generated dataset expands the scope of ML analyses, effectively addressing the aforementioned challenges in optimizing the design of strip footings on subsurfaces composed of sand over clay. Furthermore, the hybrid DFNN-WOA model enhances our predictive capabilities by optimizing complex, non-linear relationships within the dataset. WOA's efficient exploration of hyperparameter space complements DFNN's ability to extract meaningful patterns from the data, leading to more accurate predictions of bearing capacity. This integrated approach not only advances the state-of-the-art in geotechnical engineering but also underscores the potential of ML in optimizing shallow foundation designs.

To bridge the gap between advanced numerical methods and ML, this research seeks to deepen our understanding of loadbearing mechanisms in layered soil systems and facilitate precise and informed decision-making in practical engineering design applications. Furthermore, our approach focuses on developing a user-friendly predictive tool that simplifies complex analyses compared to traditional methods. By automating data generation and analysis through IGA and ML, our study streamlines the process of assessing bearing capacity in layered soil profiles. This not only improves the accuracy of predictions but also enhances practical usability, allowing engineers to make informed decisions in geotechnical design without the heavy computational demands. This effort supports the sustainable development of infrastructure in an increasingly complex world and highlights the potential for more precise and data-driven approaches to tackle longstanding challenges in geotechnical engineering.

#### 2. Problem definition

The schematic representation of the plane strain bearing capacity problem is shown in Fig. 1. In this scenario, a strip footing with a width B is positioned atop a sand layer characterized by a thickness  $H_1$ , an internal friction angle  $\varphi'$ , a unit weight  $\gamma$ , and an additional surcharge q. Beneath the sand layer lies a substantial bed of clay, possessing an undrained shear strength  $c_{uo}$  and extending to a depth  $H_2$ . Although the physical-mechanical properties of clayey soil are highly complex (Nikbakht et al., 2022), this study assumes that the shear strength of the clay increases with depth  $z_2$ , with the rate of this increase represented by the gradient  $\rho$ . It's essential to note that the analysis focuses exclusively on the short-term stability of the footing. Consequently, the sand layer is presumed to be fully drained, while the clay bed is considered undrained.

Previous investigations conducted by Shiau et al. (2003) have formulated the ultimate bearing capacity of the two-layer foundation problem in a dimensionless expression:

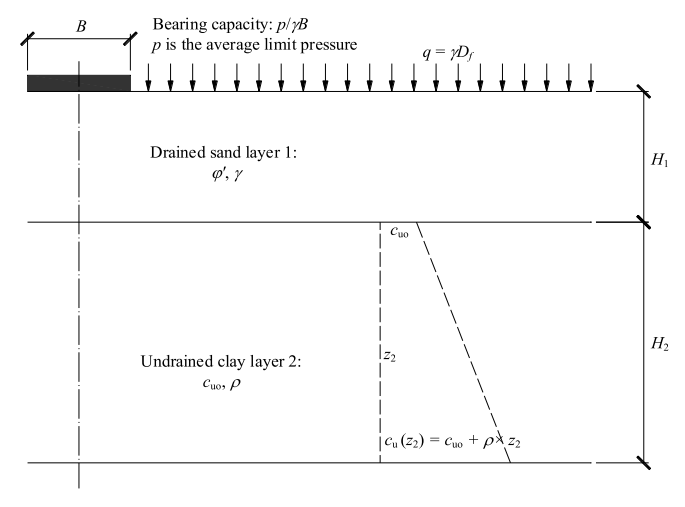


Fig. 1. Problem notation.

$$\frac{p}{\gamma B} = f\left(\frac{H_1}{B}, \frac{q}{\gamma B}, \varphi', \frac{c_{\text{uo}}}{\gamma B}, \frac{\rho B}{c_{\text{uo}}}\right) \tag{1}$$

where the average limit pressure p serves as a pivotal parameter. The expressions for the bearing capacity ratios  $(p/\gamma B)$  are presented in dimensionless terms, considering  $H_1/B$ ,  $q/\gamma B$ ,  $\varphi'$ ,  $c_{\rm uo}/\gamma B$ , and  $\rho B/c_{\rm uo}$ , with separate investigations into the influence of footing roughness. The parameter ranges adopted for the study are set as follows:  $H_1/B$  ranges from 0.125 to 2,  $q/\gamma B$  ranges from 0 to 1,  $\varphi'$  ranges from 20° to 50°,  $c_{\rm uo}/\gamma B$  ranges from 0.2 to 5, and  $\rho B/c_{\rm uo}$  ranges from 0 to 1.

This research combines IGA, UB limit analysis, and SOCP to determine the bearing capacity calculations of sand over clay. The UB solution is derived by imparting a unit downward velocity to the nodes on the footing. In cases modeling a perfectly rough foundation, these nodes are constrained to prevent horizontal movement (u=0). Conversely, for a smooth base, these nodes are allowed horizontal movement. The methodologies for UB limit analysis using simplex strain elements and SOCP were originally outlined by Makrodimopoulos and Martin in 2007. The IGA concept, introduced by Hughes et al., in 2005, is integrated into our approach. B-spline basis functions are employed to precisely model the geometry, simultaneously serving as the foundation for the solution space in line with the isoparametric concept. Further elaboration on these details will be discussed in subsequent sections.

#### 3. IsoGeometric and UB analyses

#### 3.1. Isogeometric analysis (IGA)

IGA and Finite Element Analysis (FEA) are both numerical techniques used in computational mechanics. While they share similarities such as using the isoparametric concept, there are key differences between the two approaches. IGA diverges from the conventional method by selecting a basis that precisely represents the geometry, whilst utilizing it as a foundation for approximating the required fields. In traditional FEA, the analysis follows the geometry, while in IGA, the geometry dictates the analysis.

The concept of IGA, proposed by Hughes et al. (2005), employs B-spline basis functions to construct an exact geometric model, thereby introducing a higher-order approach to FEA. For the element analysis, the bivariate B-spline basis functions  $R_{\rm I}(\xi,\eta)=R_{\rm I,j}(\xi,\eta)$  are also used to approximate the displacement fields. This is the same concept as the shape functions in a traditional FEA (Nguyen-Thoi et al., 2023; Ly et al., 2024):

$$\boldsymbol{u} = \begin{bmatrix} u \\ v \end{bmatrix} = \sum_{I=1}^{\text{ncp}} R_I(\xi, \eta) \begin{bmatrix} u_I \\ v_I \end{bmatrix} = \boldsymbol{R}(\xi, \eta) \times \boldsymbol{d} \quad (I = 1, 2, ..., ncp)$$
 (2)

where  $(u_i, v_i)$  denote the values of the displacements at the control point  $P_i(P_{i,i})$  and ncp is the number of control points.

The displacement vector  $\mathbf{d}$  of control points is stored in the following order:

$$\mathbf{d} = \begin{bmatrix} u_1 & u_2 & \dots & u_{ncp} & v_1 & v_2 & \dots & v_{ncp} \end{bmatrix}^{\mathbf{T}}$$
 (3)

Strains are therefore given by

$$\boldsymbol{\varepsilon}(\xi,\eta) = \partial \boldsymbol{R}(\xi,\eta) \times \boldsymbol{d} = \boldsymbol{B}(\xi,\eta) \times \boldsymbol{d}$$
(4)

where  $\mathbf{B}(\xi,\eta) = \partial \mathbf{R}(\xi,\eta)$  is the strain-displacement matrx, which changes with the value of  $\mathbf{R}(\xi,\eta)$ .

#### 3.2. UB analysis as SOCP

The UB analysis, formulated as SOCP by Makrodimopoulos and Martin in 2007, was briefly discussed in Nguyen-Minh et al. (2023, 2024). After introducing an approximation of the displacement and using the smoothened strains, the UB limit analysis problem for the plane strain can be formulated as

$$\lambda^{+} = \min\left(\sum_{e=1}^{\text{nel}} cA_{e}t_{e}\cos\varphi - W_{\text{ext}}^{0}(\dot{u})\right)$$
 (5a)

Subject to

$$\begin{aligned} W_{\text{ext}}(\dot{u}) &= 1 \\ \dot{u} &= 0 \ \ on \ \Gamma_u \\ \ddot{\varepsilon}_{xx}^e + \ddot{\varepsilon}_{yy}^e &= t_e sin \varphi(e=1,2,...,nel) \\ \|\rho\|_e &\leq t_e(e=1,2,...,nel) \end{aligned}$$
 (5b)

where *nel* is the number of elements in the whole investigated domain. And the fourth constraint in Eq. (5b) represents the optimization problem in the form of a SOCP problem, so that a large-scale problem can be solved efficiently.

Since strains change with the value of  $\mathbf{R}(\xi,\eta)$  (see Eq. (4)), Nguyen-Minh et al. (2024) proposed a framework to obtain the smoothed strains of IGA element e as below:

$$\dot{\tilde{\boldsymbol{\varepsilon}}} = \left[\dot{\tilde{\boldsymbol{\varepsilon}}}_{xx}^{e} \dot{\tilde{\boldsymbol{\varepsilon}}}_{yy}^{e} \dot{\tilde{\boldsymbol{\varepsilon}}}_{yy}^{e}\right]^{T} = \dot{\tilde{\boldsymbol{B}}}_{e} \boldsymbol{d}_{e} \ (\boldsymbol{d}_{e} = \text{constant})$$
 (6)

$$\dot{\tilde{B}}_{e} = \begin{bmatrix}
\dot{\tilde{R}}_{1,x} & \dot{\tilde{R}}_{2,x} & \dot{\tilde{R}}_{3,x} & \dot{\tilde{R}}_{4,x} & 0 & 0 & 0 & 0 \\
0 & 0 & 0 & \dot{\tilde{R}}_{1,y} & \dot{\tilde{R}}_{2,y} & \dot{\tilde{R}}_{3,y} & \dot{\tilde{R}}_{4,y} \\
\dot{\tilde{R}}_{1,y} & \dot{\tilde{R}}_{2,y} & \dot{\tilde{R}}_{3,y} & \dot{\tilde{R}}_{4,y} & \dot{\tilde{R}}_{1,x} & \dot{\tilde{R}}_{2,x} & \dot{\tilde{R}}_{3,x} & \dot{\tilde{R}}_{4,x}
\end{bmatrix} (7)$$

$$\overset{\dot{\sim}}{R}_{l,x} = \frac{1}{A_e} \int\limits_{\varOmega_e} \dot{R}_{l,x} d\varOmega_e \overset{\dot{\sim}}{R}_{l,y} = \frac{1}{A_e} \int\limits_{\varOmega_e} \dot{R}_{l,y} d\varOmega_e A_e$$

$$= \int_{\Omega} d\Omega_{e} \left( I = 1, 2, 3, 4 \right) \tag{8}$$

In this research, IGA is utilized for calculating internal power dissipation, where the domain  $\Omega$  is divided into nel elements. It is noteworthy that the final constraint in Eq. (5) is formulated in the quadratic form, enabling the application of the conic interior point optimizer from the academic Mosek to address the optimization problem.

### 3.3. Numerical simulation

Fig. 2 illustrates a typical UB mesh for the problem of a surface footing on a layered clay profile, incorporating the applied velocity boundary conditions. Due to the problem's symmetry, the analysis is performed with half of the region, where L=10B and  $H=H_1+H_2=5B$ . The model is represented by using B-spline basis functions with identical polynomial orders in both directions, i.e., p=q=1. The total number of elements, denoted as nel, is determined by multiplying the number of elements in the  $\xi$  and  $\eta$  directions, represented by  $n_{\rm X}$  and  $n_{\rm Y}$ , respectively.

When conducting an analysis, mesh refinement is often needed to improve solution accuracy. In IGA, this is done by knot insertion. It entails introducing new knot values between existing ones, resulting in additional elements. Noting that knot insertion does not alter either the geometry or the parametrization of the curve, instead, it increases the number of control points. The success of this process relies on a specific selection criterion for the new control points.

Fig. 3 presents a schematic of the mesh when  $nel = n_{\rm X} \times n_{\rm y} = n_{\rm X} \times (n_{\rm y1} + n_{\rm y2}) = 20 \times (4+6) = 200$  elements. Initially, there are  $nel = n_{\rm X} \times n_{\rm y} = 1 \times 2 = 2$  elements, and the number of initial control points (the red points in Fig. 3a) are  $(1+p) \times (2+q) = 6$ , where p=q=1.

The coordinates of the initial control points are detailed in Table 1. Knot insertion routines are subsequently employed to refine the mesh, resulting in 200 elements as illustrated in Fig. 3b, c, and d. For the generalization of the footing problem, the initial knot vectors are chosen:

where  $n_{v} = n_{v1} + n_{v2}$  (where  $n_{v1}$ ,  $n_{v2}$  are illustrated in Fig. 2).

The alignment of control points during mesh refinement is determined by a knot insertion routine. As the formulas are based on a single knot inserted, the routine is repeated to achieve the desired number of elements. The total number of elements for analysis is  $nel = n_x \times n_y = n_x \times (n_{y1} + n_{y2}) = 160 \times (32 + 48) = 160 \times 80 = 12,800$  elements.

The global knot vectors expand as knots are inserted:

$$\begin{cases} \text{direction} : \Xi = \{0, 0, 1, 2, ..., 158, 159, 160, 160\} \\ \eta \text{ direction} : H = \{0, 0, 1, 2, ..., 78, 79, 80, 80\} \end{cases}$$
 (10)

Finally, an element in parameter space has an area of  $[\xi_i,\xi_{i+1}] \times [\eta_j,\eta_{j+1}] = [0,1] \times [0,1]$ . Therefore, a mapping between each parent element and the parameter space is necessary for using numerical integration.

The distinct procedural approach of discretization in IGA, illustrated in Fig. 3 compared to traditional FEM, enables the proposed numerical model IGA-UB to automatically generate large datasets by systematically varying input parameters. This capability is crucial for capturing a wide range of scenarios in geotechnical analyses, particularly in complex soil profiles such as sand over clay configurations.

#### 4. Numerical results and validation

To assess the reliability of the proposed IGA-UB model, we start with Fig. 4, which compares the computed bearing capacity factors with those reported by Shiau et al. (2003) using FELA. Numerical results have shown a consistent decrease (improved UB) in bearing capacity factor ( $p/\gamma B$ ) as the number of IGA elements (nel) increases. Note the substantial agreement between the improved solutions obtained using the current IGA-UB method and those derived from FELA by Shiau et al. (2003). In addition, Table 2 further presents the convergence rate of the bearing capacity factor through the IGA-UB method. The maximum CPU time for the refined study involving 12,800 elements is approximately 20.7 s. It can therefore be concluded that the utilization of the IGA-UB analysis not only significantly reduces the size of the optimization problem but also conserves computational resources, rendering it an efficient and dependable method.

The IGA-UB method demonstrates remarkable precision through a rigorous comparison with the upper-bound and lower-bound results from Shiau et al. (2003). Importantly, the bracketed value between these bounds suggests the potential for achieving exact values. Figs. 4 and 5 clearly illustrate that the bearing capacity

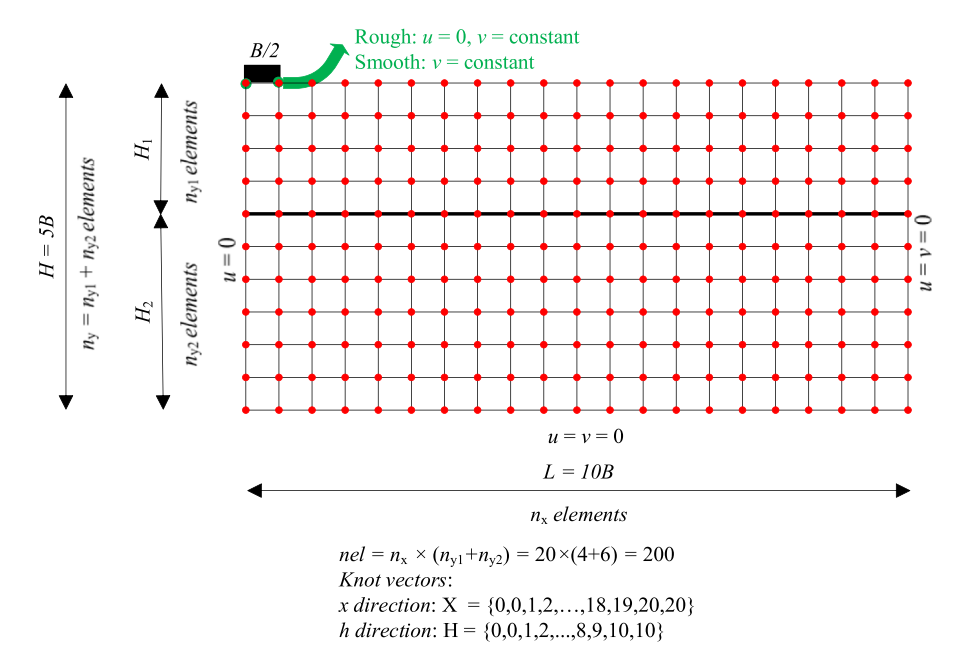


Fig. 2. IGA mesh and displacement boundary conditions in case 200 elements.

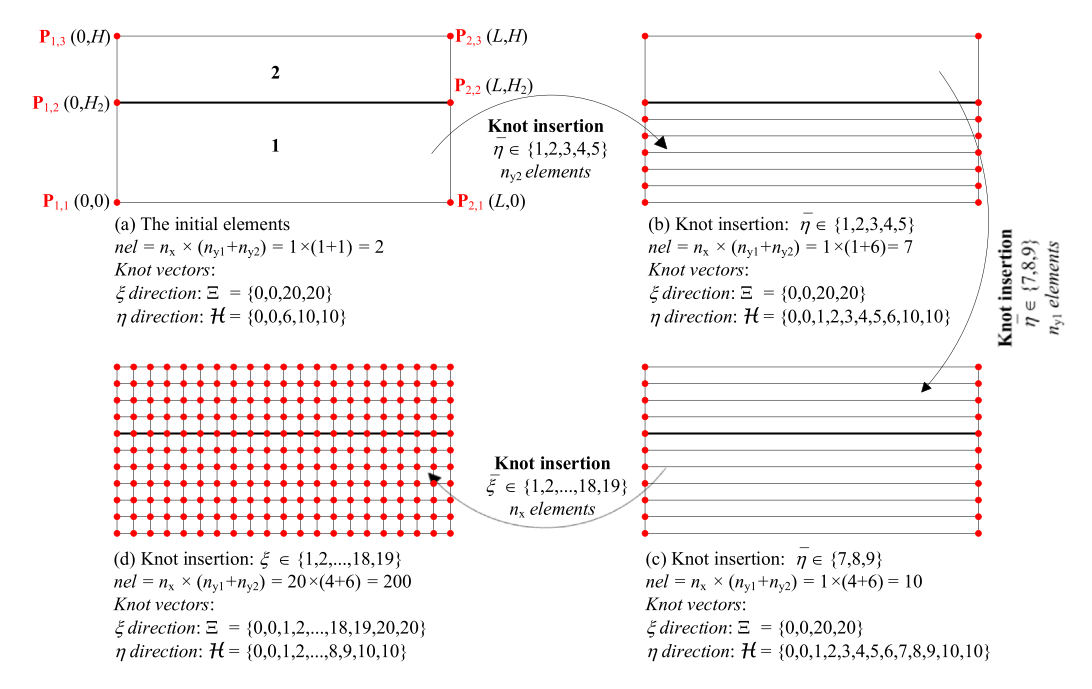


Fig. 3. Schematic of mesh: (a) The initial elements, (b), (c), (d) Knot insertion process for refinement of the mesh.

**Table 1**The coordinates of initial control points for Fig. 3.

i	$P_{i,1}(x,y)$	$P_{i,2}(x,y)$	$P_{i,3}(x,y)$
1	(0,0)	(0,H <sub>2</sub> )	(0,H)
2	(L,0)	$(L, H_2)$	(L, H)

values obtained from the proposed IGA-UB method consistently lie within the bounded range established by Shiau et al. (2003). This robust consistency not only validates the accuracy of the IGA-UB model but also highlights its capability to effectively reconcile

and refine predictions between upper and lower-bound analyses. Such alignment underscores the reliability and robustness of the IGA-UB approach in predicting bearing capacity across diverse soil conditions and geometries.

The comparison is also extended to other well-established approaches, including semi-empirical models proposed by Hanna and Meyerhof (1980), displacement FEM solutions by Griffiths (1982) and Burd and Frydman (1997), analytical kinematic predictions by Michalowski and Shi (1995), and the multi-rigid-block UB method by Maosong Huang and Hui-Lai Quin (2009). The results obtained from the IGA-UB method are consistently aligned with

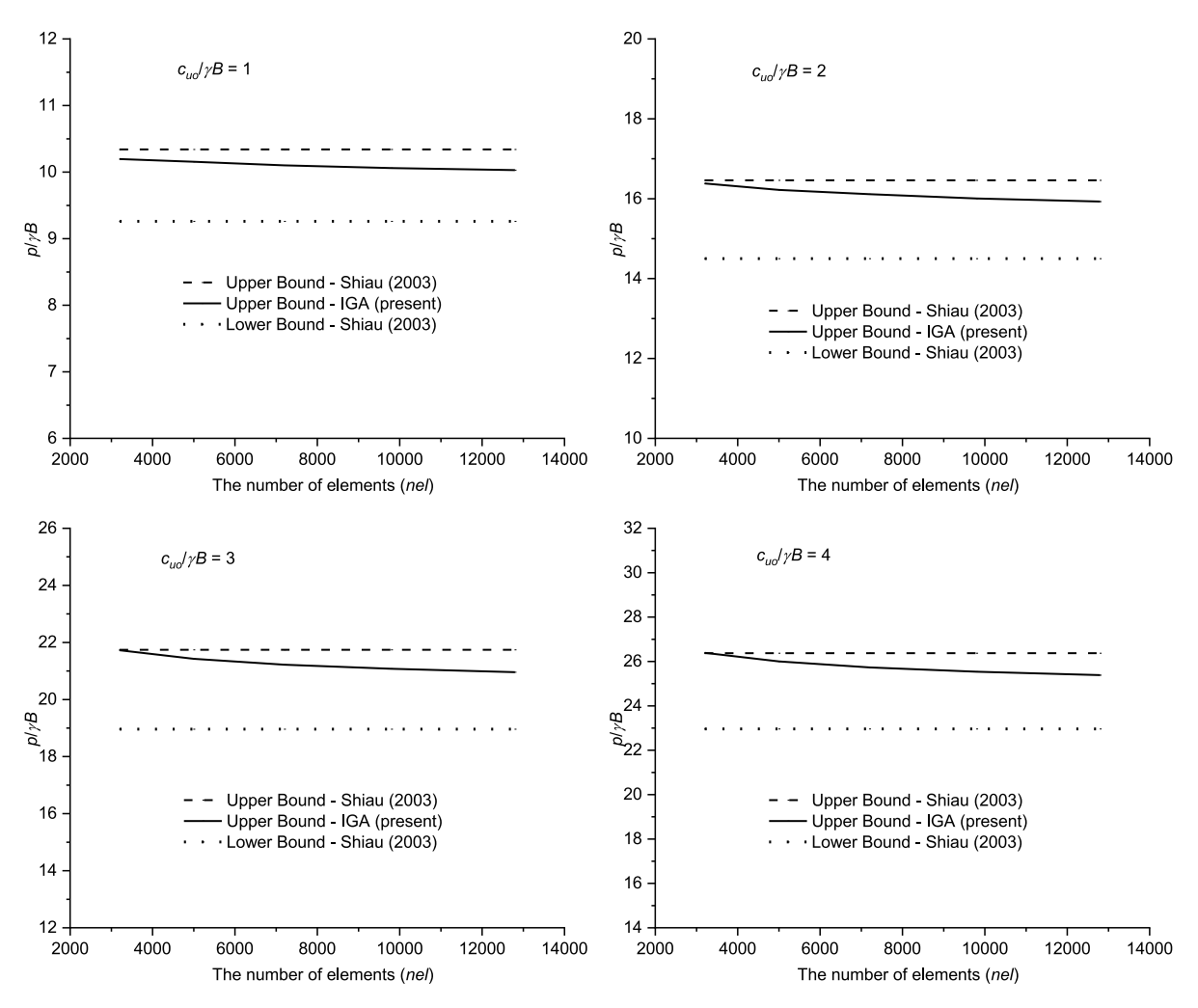


Fig. 4. Convergence rate of bearing capacity  $p/\gamma B$  between the present study and those given in Shiau et al. (2003) for  $H_1/B = 1$ ,  $q/\gamma B = 0$ ,  $\varphi' = 40^\circ$ , rough base.

**Table 2** The convergence rate of bearing capacity  $p/\gamma B$  for  $H_1/B=1$ ,  $q/\gamma B=0$ ,  $\varphi'=40^\circ$ .

$c_{\mathrm{uo}}/\gamma B$	Bearing capacity $p/\gamma B$ (Shiau et al., 2003)			Number of IGA elements ( $nel$ ); Bearing capacity $p/\gamma B$ ; CPU times ( $s$ ); Processor: Intel Core i5 (8 CPUs). Memory: 8192 MB RAM				
	LB	UB	Average	nel = 3200	nel = 5000	nel = 7200	nel = 9800	nel = 12800
1	9.26	10.34	9.8	10.196; 6.5 s	10.155; 16.4 s	10.100; 31.3 s	10.059; 67.1 s	10.028; 144.7 s
2	14.5	16.46	15.48	16.381; 7.7 s	16.219; 29.2 s	16.113; 37.1 s	16.005; 76.6 s	15.927; 204.7 s
3	18.96	21.74	20.35	21.725; 7.4 s	21.424; 14.5 s	21.217; 32.3 s	21.077; 74 s	20.957; 140.6 s
4	22.96	26.37	24.67	26.389; 7 s	26.002; 15.1 s	25.732; 33.4 s	25.534; 78.2 s	25.386; 138.2 s

those from these methodologies, as vividly depicted in Fig. 5a, b, and c.

Furthermore, the bearing capacity values from the numerical model are compared against centrifuge tests conducted by Okamura et al. (1997), as illustrated in Fig. 5d. While the results obtained from the IGA-based UB limit model are generally higher than those from the centrifuge model tests, there is a remarkable agreement between the numerical model and centrifuge tests for  $H_1/B$  ratios ranging from 0 to 3. Notably, the failure pressures calculated using the UB IGA method closely match the measured failure pressures in these scenarios. This alignment underscores the IGA method's accuracy and reliability in analyzing the layered bearing capacity problem. The demonstrated precision and robustness of the IGA method affirm its potential as a valuable tool

in geotechnical engineering practice, capable of delivering dependable results for complex soil-structure interactions.

Fig. 6 provides a direct comparative analysis with the FELA modeling conducted by Shiau et al. (2003). The plots in Fig. 6 correspond to specific conditions, including  $\varphi$ ' values of 30°, 40°, and 50°,  $q/\gamma B$  values of 0 and 1, and  $H_1/B$  ratios of 0.25, 0.5, 1, and 2 for a perfectly rough footing. It is important to emphasize that these results align exceptionally well with the averages derived from the upper and lower bound solutions proposed by Shiau et al. (2003). The consistency across different parametric ranges has significantly enhanced our confidence in the reliability and robustness of the IGA-UB study, and thus reaffirms the credibility as a valuable resource for geotechnical analyses and design considerations in the field.

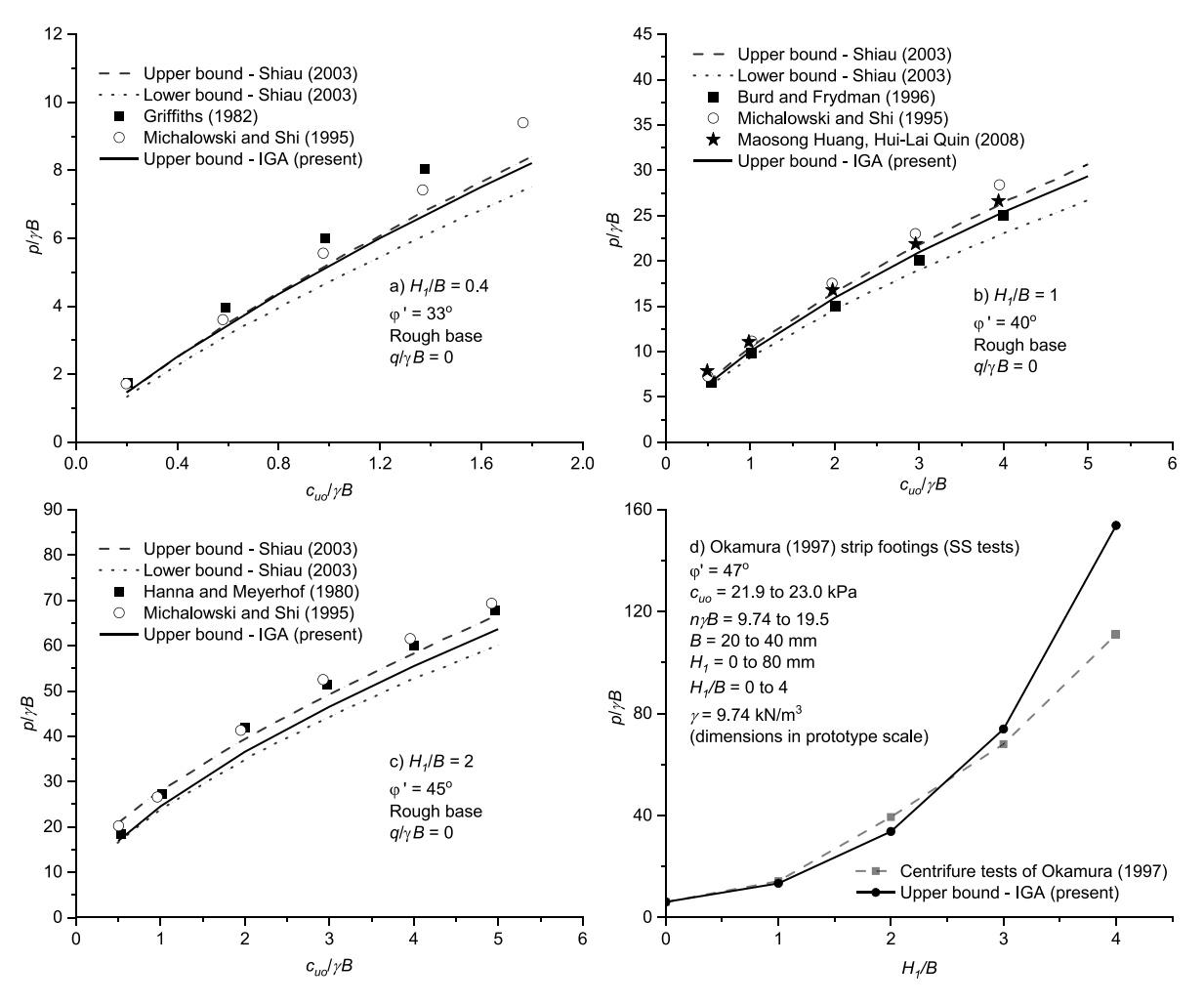


**Fig. 5.** Comparing results of bearing capacity  $p/\gamma B$ , rough footings.

The effect of footing roughness under the conditions of  $H_1/B =$ 0.5 and  $q/\gamma B = 0$  is shown in Fig. 7 for various  $\varphi$ ' values of 30°, 40°, and 50°. The comparisons affirm the excellent agreement between the two methods, in particular for the notable discrepancy between smooth and rough results in bearing capacity at  $\varphi' = 30^{\circ}$  and  $c_{110}/\gamma B$ = 4. The observed decline in bearing capacity for the smooth footing, approximately halving compared to the rough counterpart, aligns consistently with the average of the upper and lower bounds proposed by Shiau et al. (2003). As the friction angle increases, the influence of footing roughness diminishes, yielding to the dominant impact of the underlying clay layer. In practical scenarios, footing roughness typically falls between perfectly smooth and perfectly rough extremes, with an interface friction angle that commonly ranges from one-half to two-thirds of the sand friction angle. For practical uses, an average of smooth and rough results would be sufficient for design purposes.

To assess the impact of the inhomogeneity of undrained strength profiles of soft, normally consolidated clays, two scenarios with values of  $H_1/B$  equal to 0.25 and 2 are examined in Fig. 8 for the linear increase of undrained strength profile, i.e. for  $\rho B/c_{uo}$  values of 0, 0.5, and 1. Fig. 8 shows that clay inhomogeneity has the most significant effect on bearing capacity when  $H_1/B$  is small. Conversely, for a deeper layer of medium-dense sand  $(H_1/B = 2$  and  $\varphi' = 30^\circ)$  on a soft clay  $(c_{uo}/\gamma B = 1)$ , the bearing capacity remains unaffected by  $\rho B/c_{uo}$ . This is mostly due to the confined velocity

fields within the top layer, and therefore the results are independent of the value  $\rho B/c_{\mathrm{uo.}}$ 

Figs. 9–14 showcase a diverse range of failure behavior linked to specific studies on the effects of  $H_1/B$ ,  $q/\gamma B$ ,  $\varphi'$ ,  $c_{\rm uo}/\gamma B$ , and  $\rho B/c_{\rm uo}$ . Overall, the failure mechanisms align well with prior research, as evidenced by congruence with Shiau et al. (2003). We start with Fig. 9 by demonstrating the effect of  $H_1/B$  on failure mechanisms using velocity contour plots. The chosen case is for  $(q/\gamma B=0,\,\varphi'=30^\circ,\,c_{\rm uo}/\gamma B=1)$ . Results show that the effect of soft clay layer on the bearing capacity factor  $p/\gamma B$  diminishes as the value of  $H_1/B$  increases. For  $H_1/B=2$ , the non-zero velocity field is entirely contained within the sand layer, resulting in the largest value of  $p/\gamma B$  for the present study.

The effect of  $\varphi'$  on failure mechanisms is shown in Fig. 10. For the selected case with  $(H_1/B=1,q/\gamma B=0,c_{uo}/\gamma B=0.5)$ , the extent of failure zone is enlarged as  $\varphi'$  increases. Notably, the change of velocity direction across the layer boundary becomes obvious for a large value of  $\varphi'=50^\circ$ . On the other hand, as shown in Fig. 11, the increased strength ratio  $c_{uo}/\gamma B$  of clay layer results in a reduced failure zone. This is further accompanied by an increase in  $p/\gamma B$ , as the failure zone tends to be confined within the top sand layer. For the surcharge effect, it is not surprised to see the increased bearing capacity factor  $p/\gamma B$  and the enlarged failure zone as the value of  $q/\gamma B$  increases in Fig. 12. For clay inhomogeneity  $\rho B/c_{uo}$  in Fig. 13, the effect is most pronounced when  $H_1/B$  is the smallest. The same

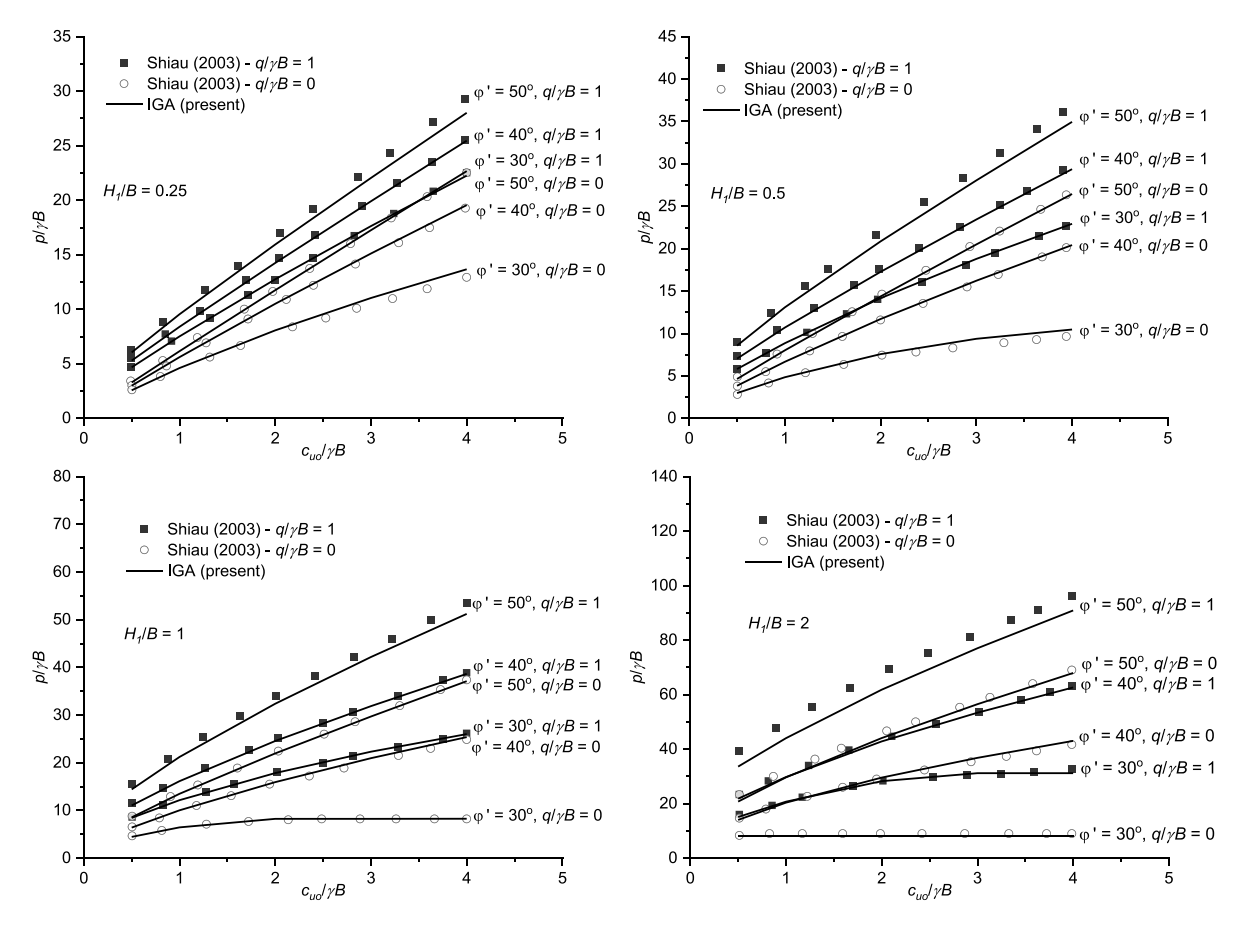


Fig. 6. Comparison of bearing capacity factor  $p/\gamma B$  between the present study and those given by Shiau et al. (2003)  $(H_1/B = 0.25, 0.5, 1, 2, \text{ rough base})$ .

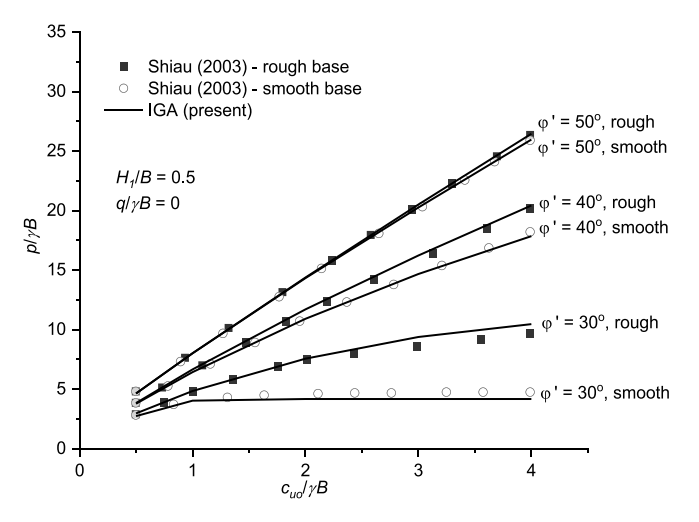


Fig. 7. Effect of footing roughness between the present study and those given Shiau et al. (2003)

observation applies to the effect of roughness, as shown in Fig. 14 for the case with  $(H_1/B=0.5, q/\gamma B=0, \varphi'=30^\circ, c_{uo}/\gamma B=4)$ .

#### 5. DNN

Fig. 15 shows the typical process of DNN method. The structure of the DNN typically comprises three essential components: the

input layer, the hidden layer, and the output layer, within which interconnected processing units are incorporated. Nonlinear transformations are applied to the input data at each layer, resulting in a distinctive representation at the output layer. Assuming that the neural network consists of V layers, with the stability number denoted as V, the output signal of the  $I^{\rm th}$  layer can be expressed as follows:

$$z_{i}^{l} = f\left(w_{i}^{T}a_{i}^{l-1} + b_{j}\right) \ \left(l = 1, 2, 3, 4, ..., V\right)$$
 (11)

The output signal at the  $l^{\rm th}$  layer in the DNN is influenced by various factors. To begin with, the activation function f is applied to the input data. Furthermore, the weight vector describes the collective impact of all units within the same hidden layer, while represents the output signal from the preceding  $(l-1)^{\rm th}$  layer. Lastly,  $b_j$  signifies the bias parameter of the  $j^{\rm th}$  unit within the current  $(l)^{\rm th}$  layer. These combined factors collectively contribute to the ultimate output signal of the DNN at each layer, consequently influencing the final prediction made by the model.

In the realm of regression problems, the meticulous selection of parameters stands as a pivotal determinant of model performance. As discussed by Nguyen et al. (2022), These vital parameters may include (i) the number of neurons; (ii) the number of layers; (iii) the activation function of choice, which includes options such as Relu, tanh, selu, and sigmoid; iv) the optimizer algorithm, offering selections like Adam, Nadam, RMSprop, and Adamax; and v) the learning rate. The optimization of these hyper parameters was conducted through the utilization of the WOA, giving rise to the development of the WOA-DNN model, a specialized framework

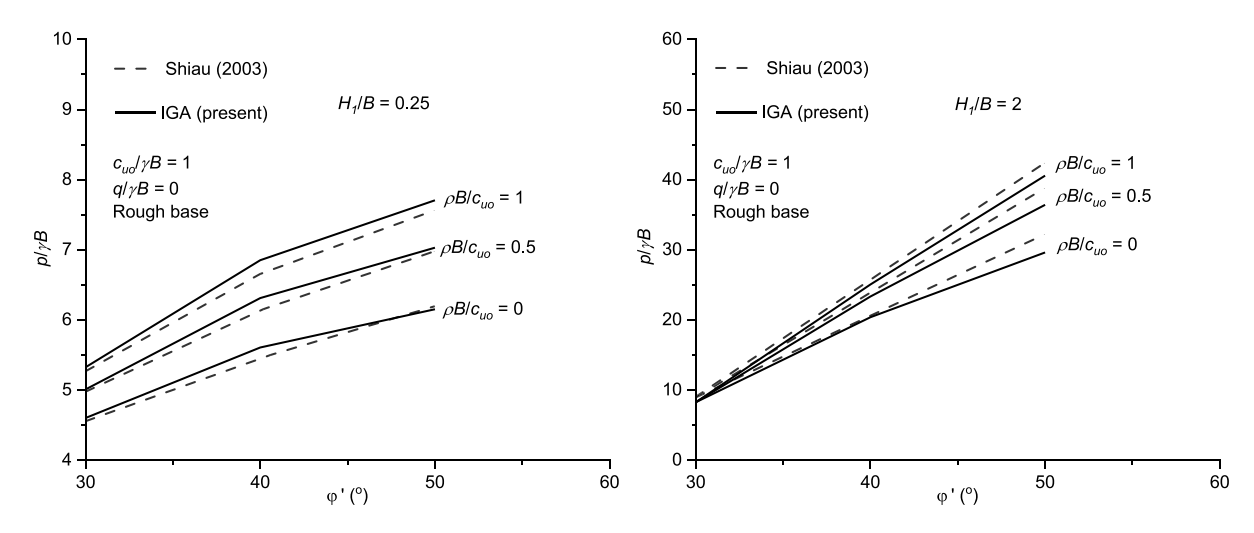
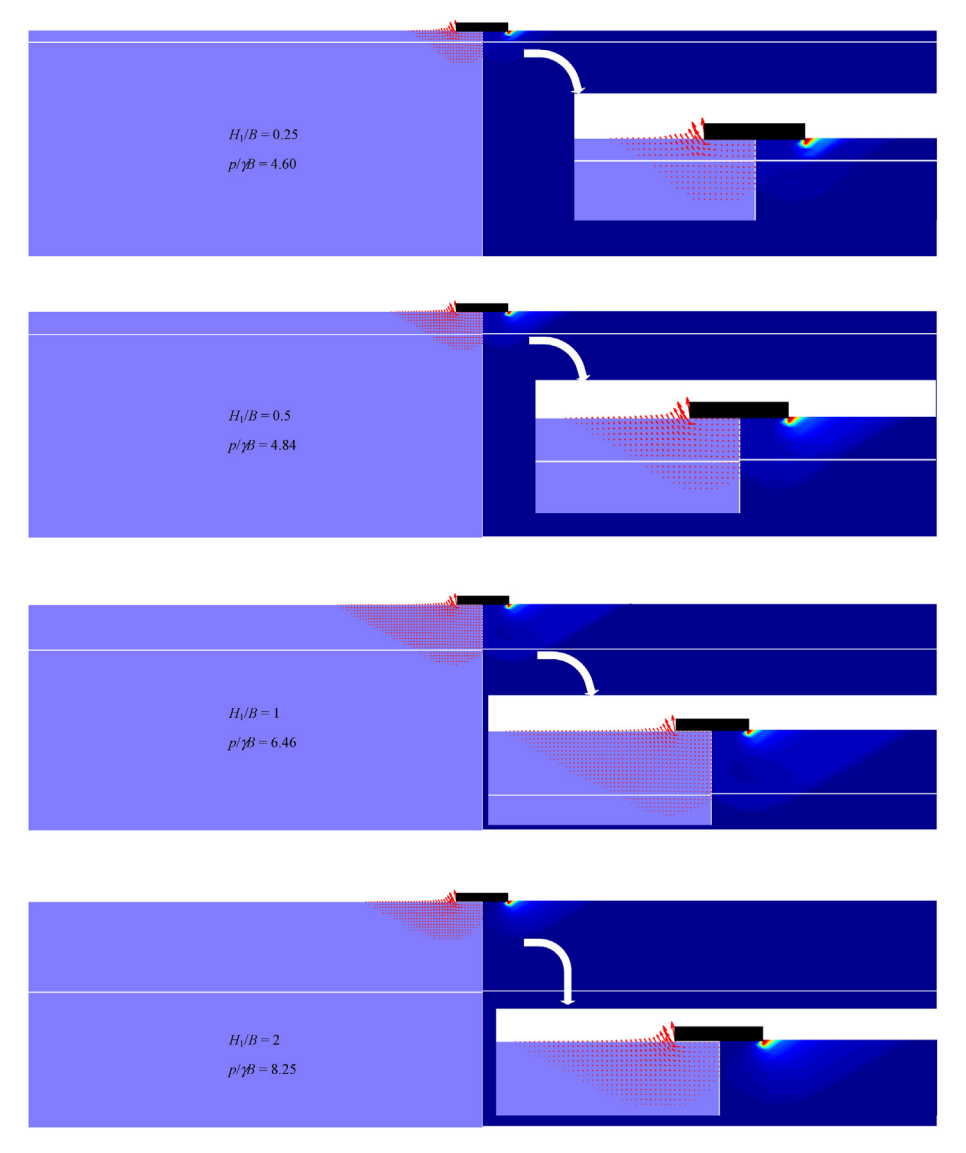
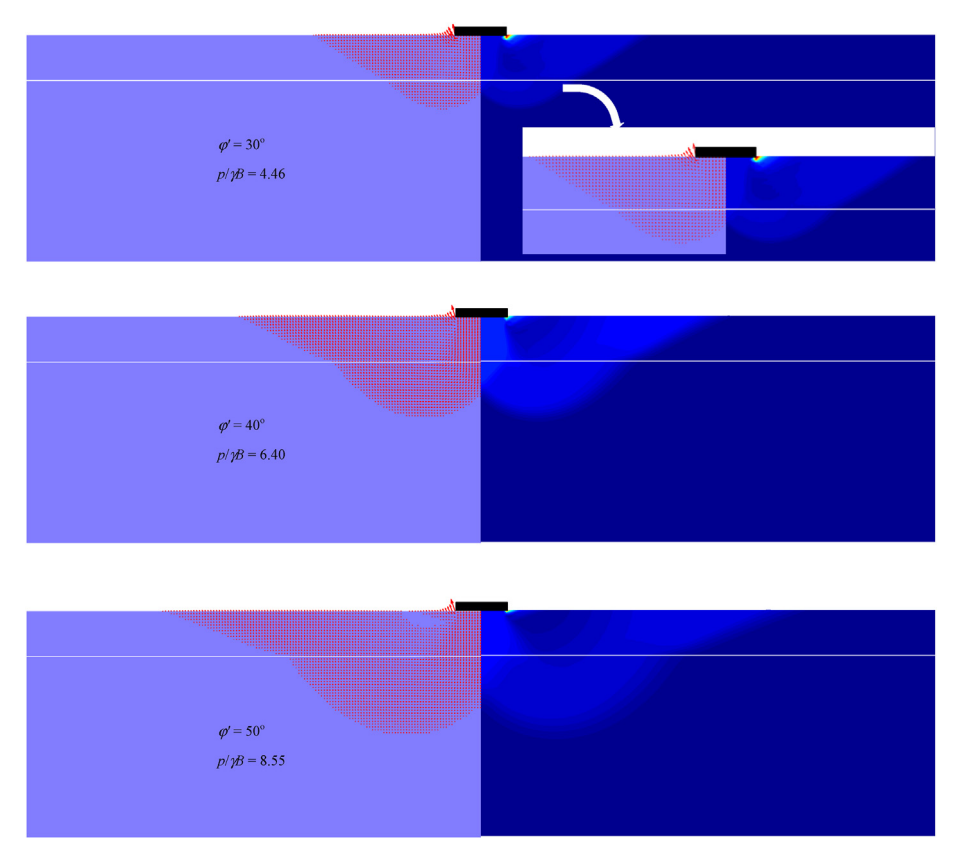


Fig. 8. Effect of increasing with depth for clay between the present study and those given in Shiau et al. (2003).



**Fig. 9.** Effect of  $H_1/B$  on failure mechanisms  $(q/\gamma B = 0, \varphi' = 30^{\circ}, c_{uo}/\gamma B = 1)$ .



**Fig. 10.** Effect of  $\varphi$ ' on failure mechanisms ( $H_1/B = 1$ ,  $q/\gamma B = 0$ ,  $c_{uo}/\gamma B = 0.5$ ).

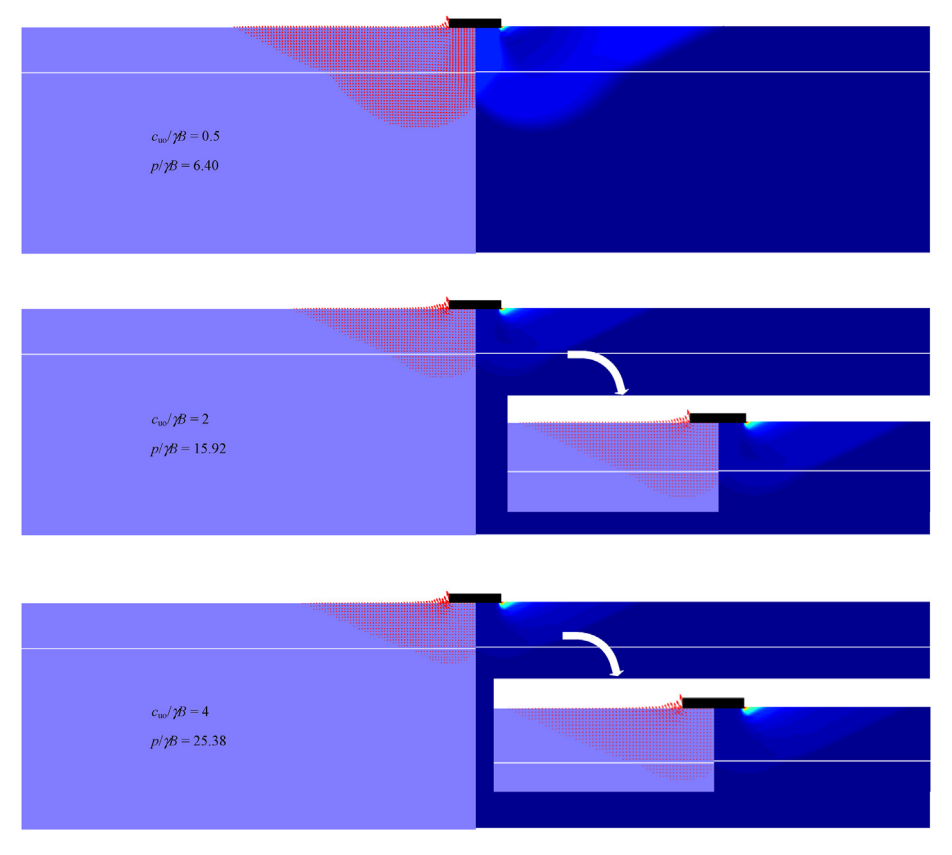


**Fig. 11.** Effect of  $c_{\rm uo}/\gamma B$  on failure mechanisms ( $H_1/B=1,\,q/\gamma B=0,\,\varphi'=40^\circ$ ).

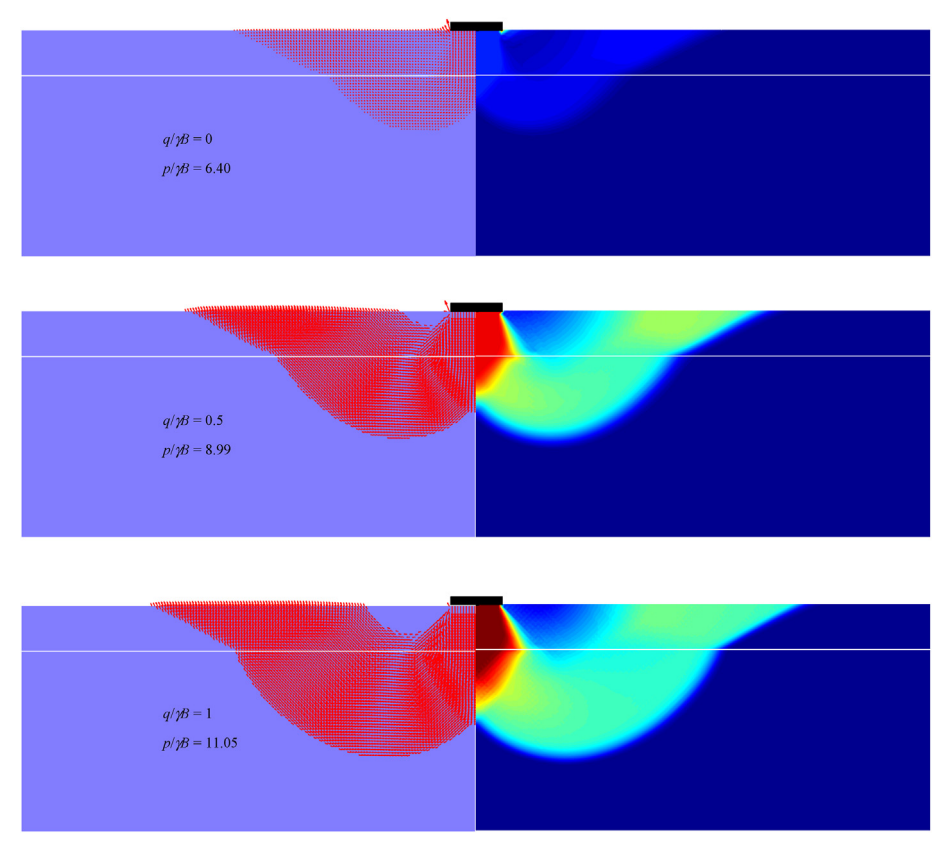


**Fig. 12.** Effect of  $q/\gamma B$  on failure mechanisms ( $H_1/B = 1$ ,  $\varphi' = 40^\circ$ ,  $c_{uo}/\gamma B = 0.5$ ).

engineered to achieve precise predictions.

In order to assess the accuracy of the model's predictions, the training regimen for the DNN involves the minimization of the loss function. In this study, the chosen loss function is Mean Square Error (MSE), a widely adopted metric for quantifying the dissimilarity between predicted and actual values. The preference for MSE arises from its straightforwardness, computational efficiency, capacity to detect outliers, and congruence with the Gaussian error distribution assumption frequently encountered in traditional DNN models (Wani et al., 2020). In addition to MSE, the model's predictive accuracy is evaluated using standard metrics such as Mean Absolute Error (MAE) and the Coefficient of Determination ( $R^2$ ). These established metrics furnish a holistic comprehension of the model's performance, providing valuable insights into predictive accuracy and identifying potential areas for further enhancement if deemed necessary.

#### 5.1. WOA

The WOA comprises three fundamental steps, namely for encircling preys, bubble-net attacking model, and searching for prey. They are discussed below (Mirjalili and Lewis, 2016).

#### 5.1.1. Encircling preys

In this step, the algorithm takes inspiration from humpback whales when they encircle their prey. As they close in on potential prey, the whales follow a spiral path and generate bubbles along the way. The underlying idea is that the randomly generated candidate solutions are expected to be in proximity to the optimal or best candidate solution. Leveraging this concept, the other candidate solutions aim to adjust their positions closer to the optimal candidate. This behavior is mathematically represented by the

following equations:

$$\overrightarrow{\boldsymbol{D}} = \left| \overrightarrow{\boldsymbol{C}} \cdot \overrightarrow{\boldsymbol{X}^*}(\boldsymbol{t}) - \overrightarrow{\boldsymbol{X}}(\boldsymbol{t}) \right| \tag{12}$$

$$\overrightarrow{X}(t+1) = \overrightarrow{X^*}(t) - \overrightarrow{A} \cdot \overrightarrow{D}$$
 (13)

where (t) represents the current iteration;  $\overrightarrow{X}^*(t)$  denotes the position vector of the best solution obtained thus far;  $\overrightarrow{X}(t)$  signifies the position vector at the current iteration;  $\overrightarrow{I}$  represents the absolute value, and "." signifies element-wise multiplication. It is essential to note that  $\overrightarrow{X}^*$  should be updated whenever a superior solution is discovered during each iteration.

Vectors  $\overrightarrow{A}$ ,  $\overrightarrow{C}$  represent coefficient vectors and are computed as follows:

$$\overrightarrow{A} = 2\overrightarrow{a} \cdot \overrightarrow{r} - \overrightarrow{a} \tag{14}$$

$$\overrightarrow{\mathbf{C}} = 2\overrightarrow{\mathbf{r}} \tag{15}$$

where  $\vec{a}$  linearly decreases from 2 to 0 over the course of iterations encompassing both exploration and exploitation phases. The vector  $\vec{r}$  is a random vector within the range [0,1].

#### 5.1.2. Bubble-net attacking model

Fig. 16 illustrates the mathematical models for the Shrinking Encircling and Spiral Updating Position mechanisms, which emulate the Bubble-Net Attacking method inspired by humpback whales. The Shrinking Encircling mechanism operates by reducing

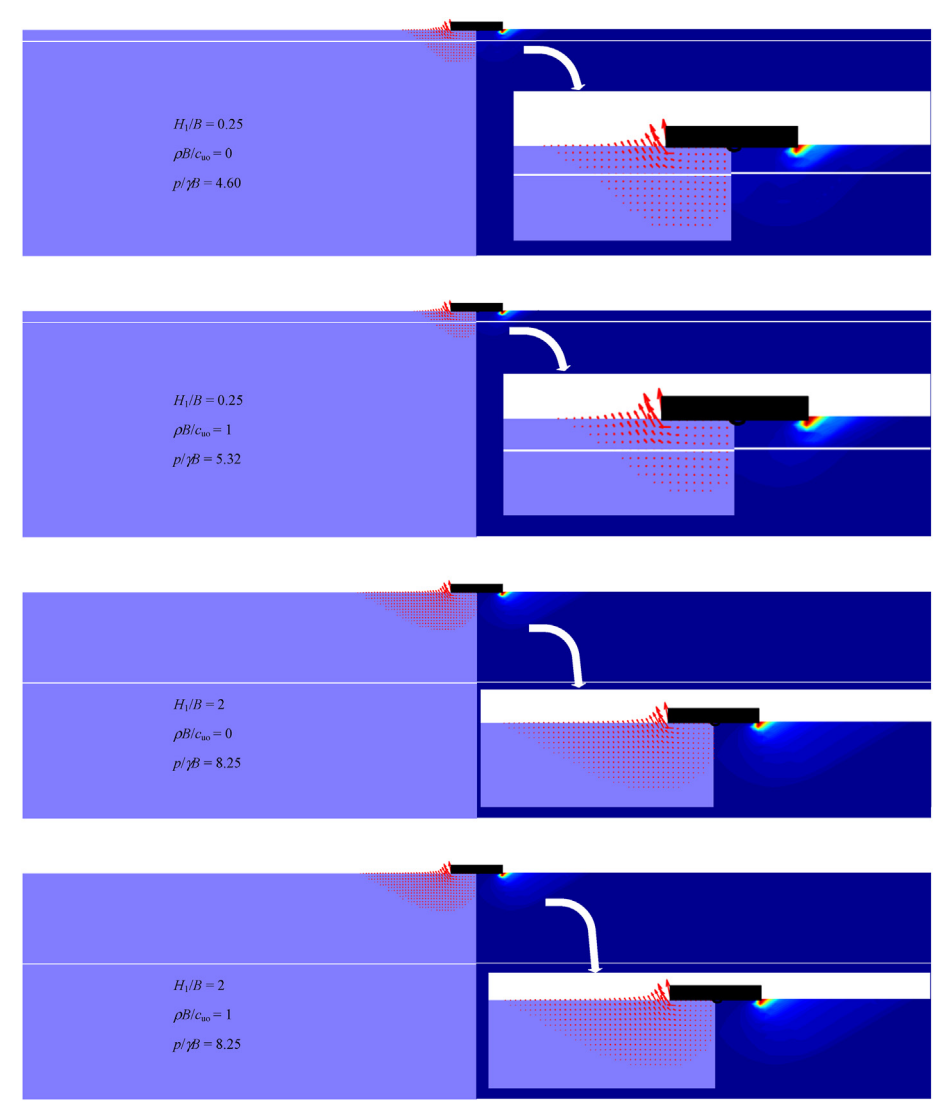


**Fig. 13.** Effect of  $\rho B/c_{uo}$  on failure mechanisms  $(q/\gamma B=0,\,\varphi'=30^\circ,\,c_{uo}/\gamma B=1).$ 

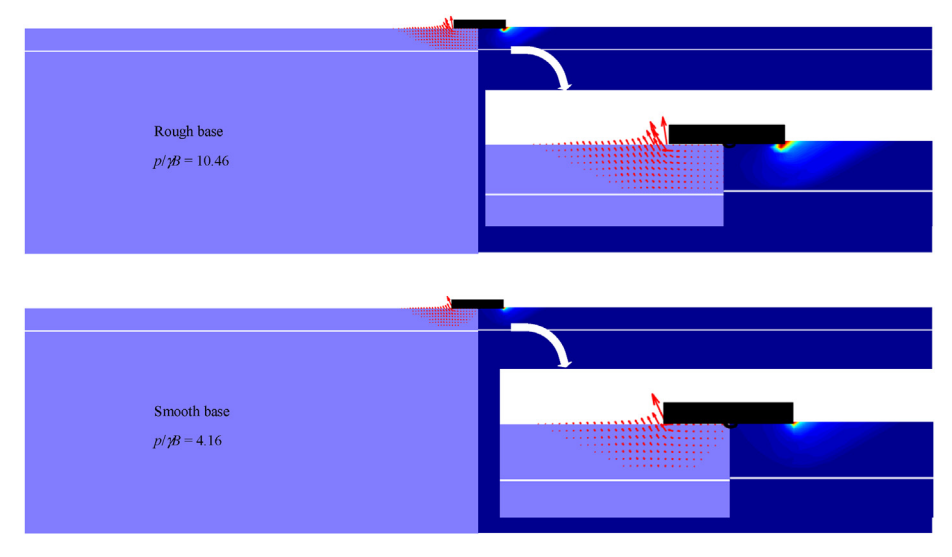


**Fig. 14.** Effect of footing roughness on failure mechanisms ( $H_1/B=0.5$ ,  $q/\gamma B=0$ ,  $\varphi'=30^\circ$ ,  $c_{uo}/\gamma B=4$ ).

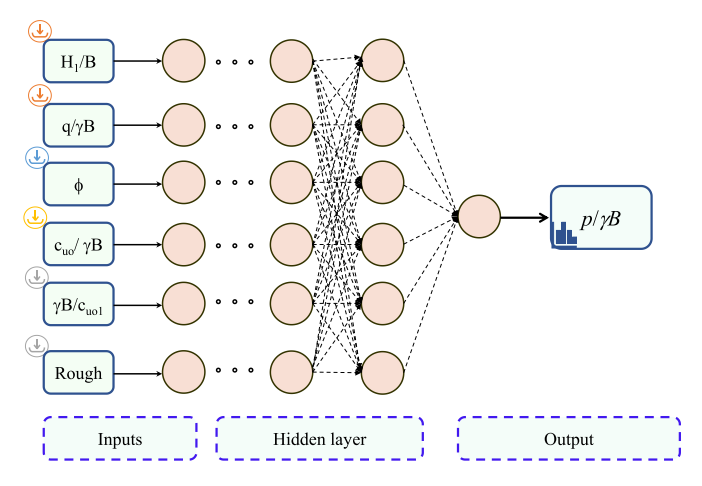


Fig. 15. Typical topology of deep neural networks.

the value of vector  $\overrightarrow{a}$  throughout the iterations, as described in Eq. (14). It's important to note that the fluctuation range of vector  $\overrightarrow{A}$  is also decreased alongside vector  $\overrightarrow{a}$ . In other words,  $\overrightarrow{A}$  becomes a random value within the interval [-a, a]. By setting random values for  $\overrightarrow{A}$  in the range [-1, 1], the candidate solution's new position is updated between its current position and the best position obtained so far.

In Fig. 16b, the distance between the whale's position (X, Y) and the prey's position  $(X^*, Y^*)$  is initially calculated. A spiral equation is then created to mimic the helix-shaped movement of humpback whales, and it is defined as follows:

$$\overrightarrow{D'} = \left| \overrightarrow{X^*}(t) - \overrightarrow{X}(t) \right| \tag{16}$$

$$\overrightarrow{X}(t+1) = \overrightarrow{D'} \cdot e^{bl} \cdot \cos(2\pi l) + \overrightarrow{X^*}(t)$$
(17)

where b represents a constant that defines the shape of the logarithmic spiral, l is a random number within the interval [-1, 1], and "•" denotes element-by-element multiplication.

Humpback whales exhibit the behavior of swimming around their prey within a shrinking circle while also following a spiral-shaped path. This behavior is simulated in the model by assuming a 50% probability to choose between the Shrinking

Encircling mechanism or the Spiral model to update the position of the whales during optimization. The mathematical model is defined as follows:

$$\overrightarrow{X}(t+1) = \begin{cases} \overrightarrow{X}^*(t) - \overrightarrow{A} \cdot \overrightarrow{D} & \text{if } p < 0.5\\ \overrightarrow{D}' \cdot e^{\text{bl}} \cdot \cos(2\pi l) + \overrightarrow{X}^*(t) & \text{if } p \ge 0.5 \end{cases}$$
(18)

where p is a random number in the range [0,1].

#### 5.1.3. Searching for prey

To search for prey, a similar approach to the Shrinking Encircling mechanism is applied. However, in this case, the  $\overrightarrow{A}$  vector with  $|\overrightarrow{A}|$ 

>1 is utilized, and the position  $\overline{X_{\rm rand}}$  of a randomly selected whale from the current population replaces the position  $\overrightarrow{X^*}(t)$  of the best candidate solution. This means that the whale can move far away from the reference whale, emphasizing exploration and enabling the WOA algorithm to perform a global search. The mathematical model is expressed as follows:

$$\overrightarrow{\boldsymbol{D}} = \left| \overrightarrow{\boldsymbol{C}} \cdot \overrightarrow{\boldsymbol{X}}_{\text{rand}} - \overrightarrow{\boldsymbol{X}}(\boldsymbol{t}) \right| \tag{19}$$

$$\overrightarrow{X}(t+1) = \left| \overrightarrow{X_{\text{rand}}} - \overrightarrow{A} \cdot \overrightarrow{D} \right|$$
 (20)

where  $\overrightarrow{X_{rand}}$  represents the position vector of a whale chosen randomly from the current population.

Some of the possible positions around a particular solution with  $|\overrightarrow{A}| > 1$  is depicted in Fig. 17.

Fig. 18 illustrates the graphical methodology of the proposed WOA-DNN. As discussed earlier, IGA's discretization facilitated automatic and random data generation using the MATLAB parfor loop, significantly reducing data generation time. Each input parameter was randomly sampled within specified ranges outlined in the manuscript, ensuring a diverse dataset that covers realistic variations encountered in practical applications. This efficient data generation enabled the creation of a large, varied dataset crucial for robust training of the WOA-DNN model. This dataset enhances the model's capability to capture complex patterns and dependencies, ensuring accurate predictions of bearing capacity in layered soil profiles.

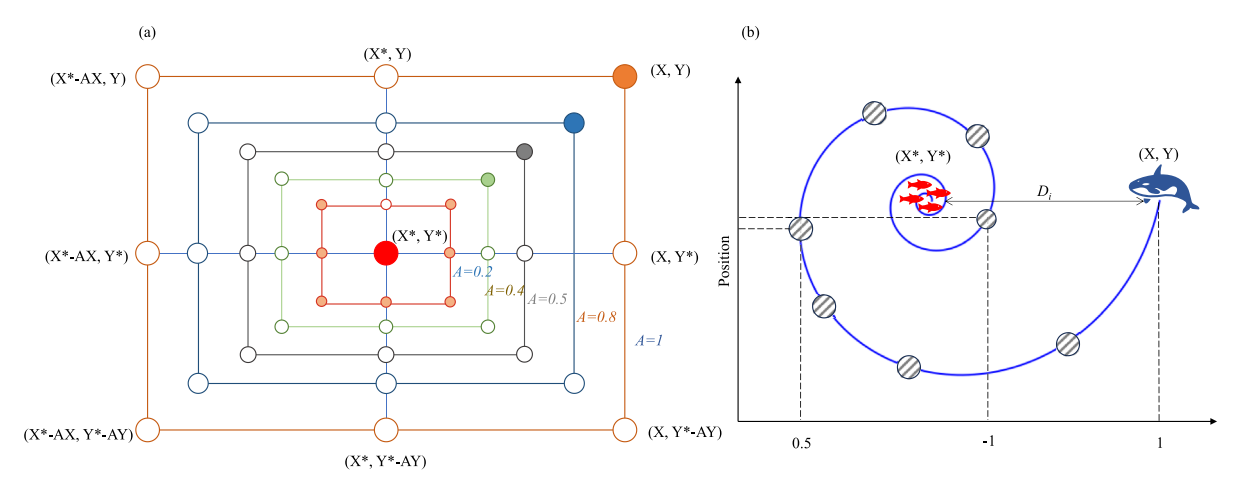


Fig. 16. Mathematical Models for Position Update Mechanisms: a) the shrinking encircling mechanism; b) the spiral updating position mechanism.

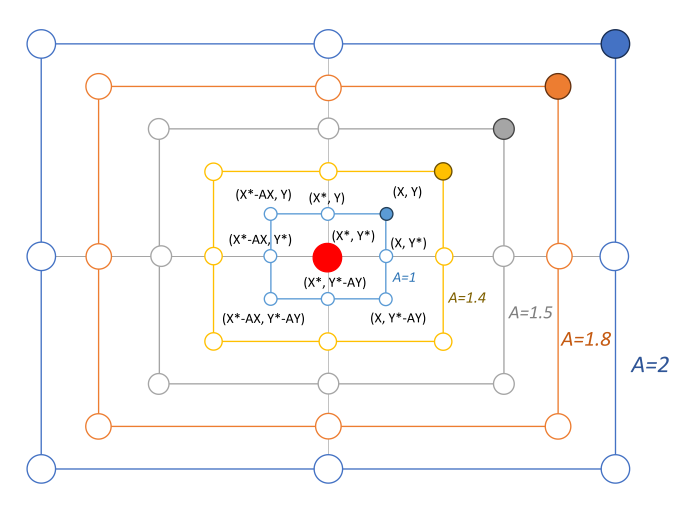


Fig. 17. Exploration mechanism implementation of WOA algorithm.

#### 5.2. Data acquisition and model development

#### 5.2.1. Preprocessing data

The bearing capacity dataset for sand on clay profile has a total of 10,000 samples. Table 3 presents an extensive statistical summary of both the input and output variables employed in this dataset. These statistical attributes are fundamental for

comprehending the dataset's underlying characteristics, offering a foundational reference for dataset analysis and interpretation. The input variables ( $X_1$  to  $X_6$ ) demonstrate a broad range of values; whereas, the means and standard deviations provide valuable insights into the central tendency and dispersion of these variables. Particularly noteworthy is the skewness of these variables, all of which are approximately zero. This proximity to zero indicates that the data is fairly symmetrically distributed and does not exhibit significant skewness in either direction.

Conversely, when we examine the output variable (Y), i.e., the bearing capacity ( $p/\gamma B$ ), a more constrained range is observed. The bearing capacity factor varies from a minimum of 1.18133 to a maximum of 96.58333. The mean value of 17.80979 indicates that, on average, the bearing capacity factor centers around this value. The standard deviation, at 16.30221, underscores the variability of these values around the mean. It's important to note the negative skewness value (-1.34078), which implies a slight leftward tail in the distribution. This suggests that some lower values deviate from the overall trend, indicating that there may be instances with bearing capacity factors significantly below the mean.

This comprehensive statistical description provides insights into the data's central tendencies, variabilities, and distribution shapes, facilitating informed analysis and interpretation. It serves as a crucial reference point for understanding the dataset's distribution and characteristics, further enhancing its utility for investigating this stability problem.

Further, the dataset undergoes a normalization process,

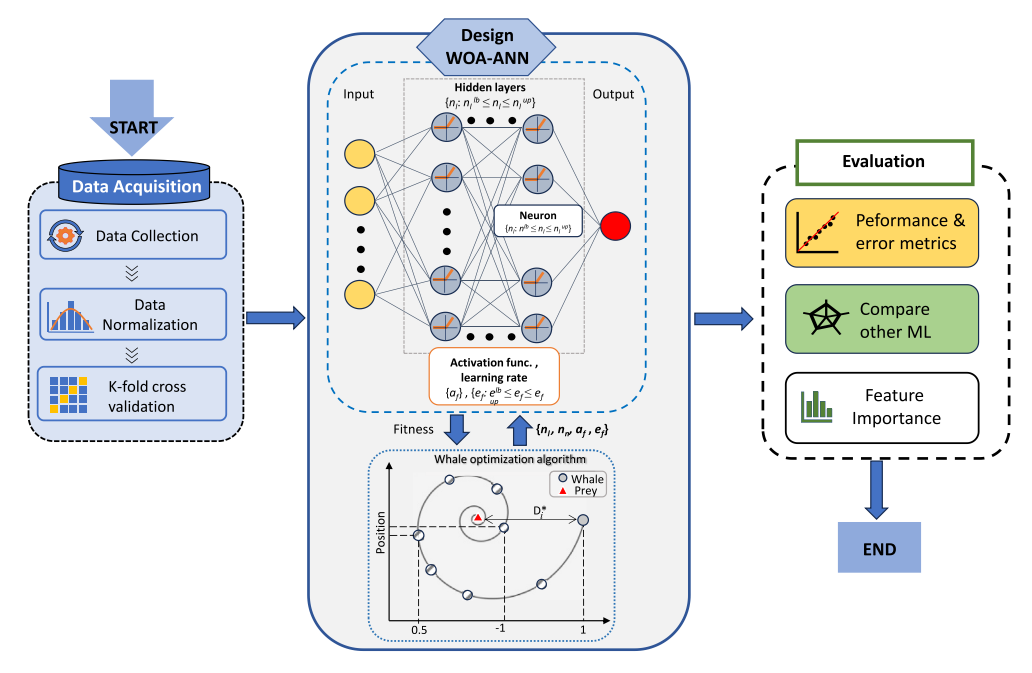


Fig. 18. The graphical methodology of the proposed WOA-DNN.

**Table 3**The statistical description of the input and output variables.

Variables	Unit	Notation	Min	Mean	Std	Skewness	Max
H <sub>1</sub> /B	_	$X_1$	0.12578	1.08398	0.54532	-0.03121	1.99940
$q/\gamma B$	_	$X_2$	0.00009	0.50104	0.28867	-0.01256	0.99979
$\varphi$ '	_	$X_3$	20.00145	35.00181	8.63392	-0.00014	49.98221
$c_{\rm uo}/\gamma B$	_	$X_4$	0.20034	2.59182	1.38300	0.00778	4.99891
$\rho B/c_{\rm uo}$	_	$X_5$	0.00007	0.49289	0.28991	0.02874	0.99984
Roughness	_	$X_6$	0.00000	0.50000	0.50000	0.00000	1.00000
$p/\gamma B$	_	Y	1.18133	17.80979	16.30221	-1.34078	96.58333

accomplished with the Minmaxscaler function, scaling the data within the range (0,1) prior to DNN model training. The distribution and statistical characteristics of each feature are presented in Fig. 19, providing valuable insights into the data's properties. Moreover, an examination of variable correlations has also been conducted. See Fig. 20 for a heatmap visualization. The results obtained from this analysis emphasize the paramount influence of the variable " $\varphi$ " on bearing capacity prediction, highlighting its pivotal role in the predictive model. Following closely is " $c_{uo}/\gamma B$ ", displaying a correlation coefficient of 0.44. Additionally, variables " $H_1/B$ " and " $q/\gamma B$ " exhibit correlations of 0.34 and 0.23, respectively, indicating their moderate yet notable contributions to the bearing capacity prediction.

Conversely, the variables " $\rho B/c_{uo}$ " and "roughness" demonstrate minimal impact on bearing capacity prediction, with correlation values approaching zero, specifically at 0.05. This suggests that their influence on the predictive model is negligible, making them relatively less critical in determining bearing capacity.

#### 5.2.2. Model development

To ensure the reliability and robustness of the model performance, a rigorous 10-fold cross-validation technique is applied. The WOA-DNN is utilized to optimize hyperparameters for accurate predictions. This technique serves a dual purpose — it provides a robust assessment of the model's performance and offers a valuable platform for fine-tuning model hyperparameters. This approach would ensure that the predictive model is well-optimized and capable of delivering accurate and dependable results. These hyperparameters include: (i) Number of neurons in the range [5, 100], (ii) Number of layers in the range [1, 4]; (iii) Activation functions: Relu, tanh, selu, sigmoid, (iv) Optimizer algorithms: Adam, Nadam, RMSprop, Adamax, and (v) Learning rate in the range [0.01, 0.5].

Through the WOA, the optimal hyperparameters are determined as follows: number of neurons = 100; number of layers = 4; activation function = 'Relu'; optimization algorithm = 'Adamax'; and learning rate = 0.01.

The performance of the proposed WOA-DNN model is systematically compared with that of an Artificial Neural Network (Nguyen et al., 2023, 2024; Van Tran et al., 2024), Light Gradient Boosting (LGB) (Ke et al., 2017), Extremely Gradient Boosting (XGB) (Chen and Guestrin, 2016), and CatBoost (Prokhorenkova et al., 2018). The details of each model's parameters are given in Table 4.

Regarding the influence of hunting party size, we showcase the convergence curves in Fig. 21 for WOA-DNN with varying hunting party sizes set at 10, 15, 20, 25, and 30, after 50 iterations. In general, all scenarios display a decreasing trend in stability beyond the  $20^{\rm th}$  iteration, with the hunting party of 30 exhibiting the most favorable performance. Notably, all these scenarios successfully achieve a remarkable level of precision, as evidenced by the objective functions converging to an impressive accuracy of  $10^{-5}$ .

In summary, the optimization of the DNN topology through the WOA results a neural network comprising 100 neurons distributed across 4 layers. This network employs the Rectified Linear Unit (ReLU) activation function, the Adamax optimizer algorithm, and a learning rate set at 0.01.

## 5.3. Results and discussion

Table 5 presents a comparison of evaluation metrics between the WOA-DNN and other models. To assess the performance of the WOA-DNN model against conventional ML techniques, we focused on key criteria of model accuracy and generalization. The network architecture parameters were optimized using WOA to enhance training efficiency, accuracy, and to mitigate underfitting and overfitting. Subsequently, the model's performance was rigorously evaluated using standard metrics including MSE, MAE, and  $R^2$ . K-fold cross-validation was employed to ensure robust performance evaluation across different subsets of the data, validating the model's ability to generalize effectively.

WOA-DNN achieved an exceptionally low MSE of 0.000 on the test dataset, surpassing all other models compared in Table 5. This minimal error indicates that WOA-DNN closely fits the actual data points with minimal prediction variance, demonstrating its superior predictive capability. In contrast, models such as LGB, XGB, CatBoost, and the standard ANN exhibited higher MSE values, suggesting less accurate predictions compared to WOA-DNN.

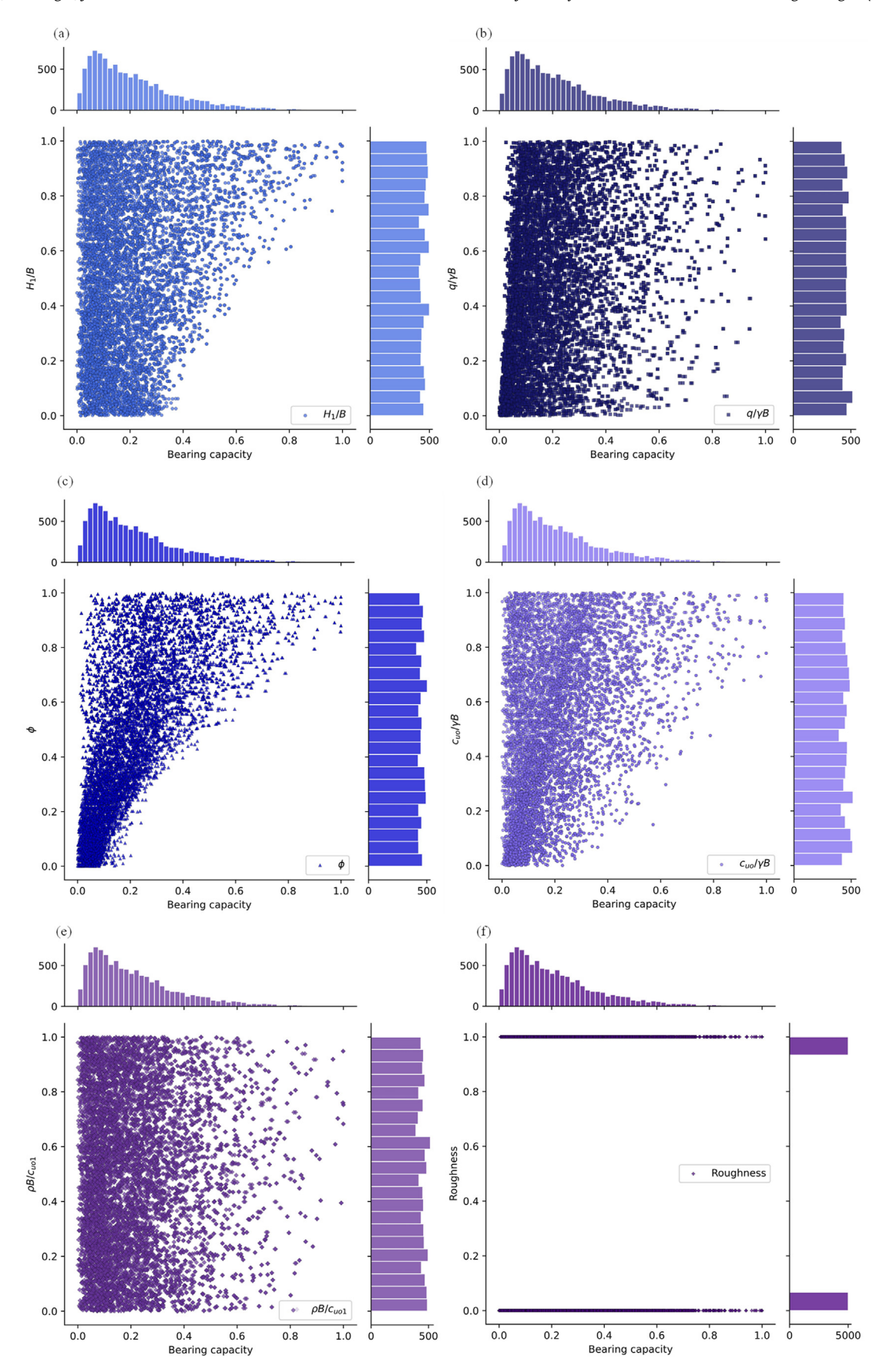
The MAE of WOA-DNN on the test dataset is an impressive 0.003, which is the lowest among all models. MAE measures the absolute difference between predicted and actual values and is a key indicator of model accuracy. This remarkable accuracy is in stark contrast to other models, which generally have higher MAE values, emphasizing WOA-DNN's superiority in providing precise predictions. The  $R^2$  value (Coefficient of Determination) of WOA-DNN is 0.999, which is the highest among all models, indicating that its predictions exhibit the highest correlation with the actual values on the test dataset. This level of predictability sets WOA-DNN apart from the other models, which though performing well, do not match the precision achieved by WOA-DNN.

Fig. 22 presents regression plots of five different machinelearning models. The models under consideration are XGB. Cat-Boost, LGB, ANN, and the WOA-DNN. This visual representation allows for a clear evaluation of each model's predictive accuracy and how well it fits the actual data. Results show that WOA-DNN stands out as the best model with the most accurate predictions. It closely follows the actual data points, resulting in a regression line that aligns almost perfectly with the data. This is a testament to WOA-DNN's remarkable accuracy in estimating the bearing capacity of strip footings on layered soils. On the other note, the other models LGB, XGB, and CatBoost, exhibit regression lines that deviate to a greater extent from the actual data points. While they perform well, they do not match the level of accuracy achieved by WOA-DNN. This visual representation reinforces the numerical results previously presented in Table 5, emphasizing that WOA-DNN surpasses the other models in providing precise and reliable predictions for the given dataset.

Fig. 23 further demonstrates the exceptional performance of the proposed WOA-DNN using the plots of residual value densities for the five models. The figure clearly emphasizes the strengths of each model, with particular attention to the densities of residual values. The plot for WOA-DNN shows a remarkable concentration of residual values around zero, with the highest maximum density of 1.2. This is a significant indicator of the model's exceptional accuracy. It consistently delivers highly precise predictions with minimal deviations from actual values. On the other hand, the other models, including XGB, CatBoost, LGB, and ANN, exhibit a broader spread of residual values with lower maximum densities. This highlights that the proposed WOA-DNN model surpasses its counterparts in providing more accurate and reliable predictions.

The key findings regarding the accuracy of the WOA-DNN model in predicting the bearing capacity of strip footings are significant. The WOA-DNN model demonstrated high accuracy with low MSE and MAE values, alongside consistently high  $R^2$  values, indicating precise predictions. Compared to conventional ML techniques, it showed superior accuracy by effectively capturing complex patterns within the data. The model's adaptability in optimizing hyperparameters using the WOA allowed for fine-tuning critical parameters, thereby enhancing its predictive capability.

Furthermore, through rigorous k-fold cross-validation across various material and geometrical scenarios, the WOA-DNN model



**Fig. 19.** Distribution of Each Variable Normalized in the range [0, 1]: (a)  $H_1/B$ , (b)  $q/\gamma B$ , (c)  $\varphi'$ , (d)  $c_{uo}/\gamma B$ , (e)  $\rho B/c_{uo}$ , and (f) Roughness.

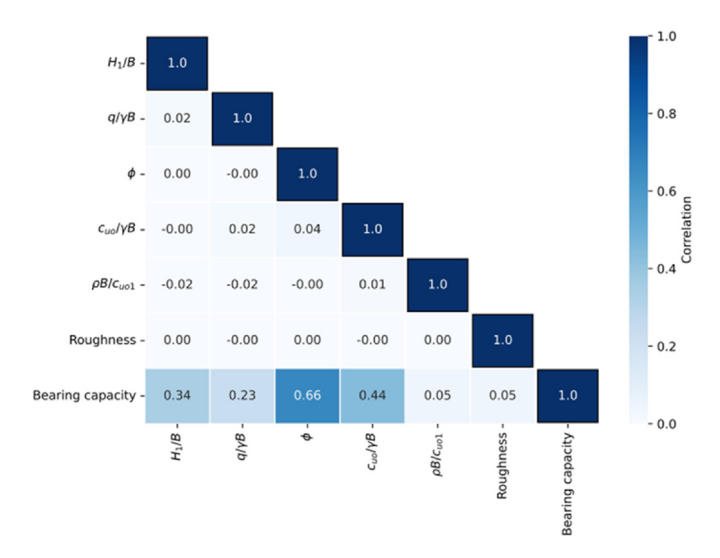


Fig. 20. Correlation of variables.

exhibited robustness and ensured reliable performance under diverse conditions. Evaluating its performance across different scenarios of sand layer depth, load-to-soil unit weight ratio, internal friction angle, cohesion, and footing roughness, the WOA-DNN demonstrated strong predictive capabilities and adaptability. This resilience stems from the diverse dataset generated through random sampling of these parameters, ensuring comprehensive coverage of material and geometrical conditions. Consistently achieving high accuracy and reliability, as confirmed by performance metrics and cross-validation results, underscores the model's effectiveness. These findings highlight the WOA-DNN's potential to accurately predict bearing capacity for layered soil profiles by accommodating diverse parameter combinations effectively.

In conclusion, the optimized architecture facilitated by the WOA not only significantly improves predictive accuracy but also enables robust generalization to unseen data, as validated through k-fold cross-validation. This technique involves partitioning the dataset into k subsets, training the model on k-1 subsets, and validating it on the remaining subset, iteratively repeating this process with different validation subsets. By evaluating the model's performance across multiple folds, we confirmed that WOA-DNN maintains resilience to variations in the training data while sustaining high precision. These findings underscore the effectiveness of WOA-DNN in modeling intricate relationships within geotechnical datasets, particularly in predicting bearing capacity for layered soil profiles. By minimizing prediction variance and providing reliable estimates across diverse soil configurations, WOA-DNN emerges as a promising tool for advancing predictive accuracy and enhancing decision-making in geotechnical engineering applications.

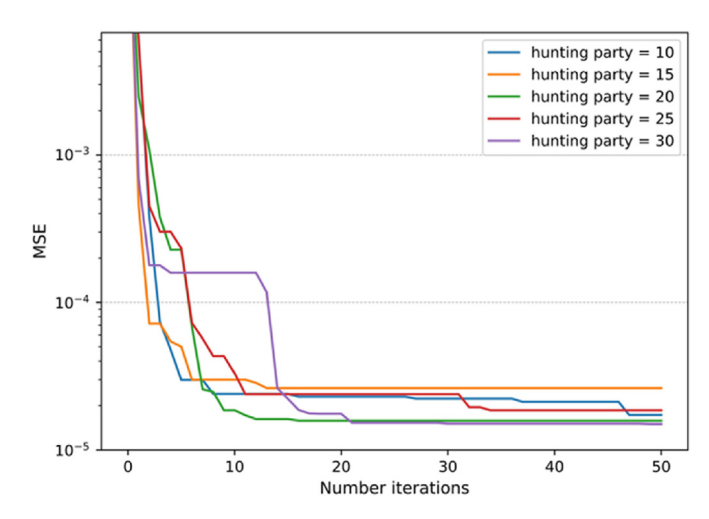


Fig. 21. Convergence curve of different hunting party value on the objective functions.

#### 6. Feature importance

#### 6.1. SHapley additive exPlanations

The Shapley values are often used to shed light on the significance of each feature in predicting soil stability. In Fig. 24, among the six variables,  $\varphi$ ' stands out with the highest SHAP value, reaching approximately 0.1. Following closely is  $c_{\rm uo}/\gamma B$ , which contributes significantly with a SHAP value of approximately 0.06.  $H_1/B$  plays a notable role with a SHAP value of 0.05, while  $q/\gamma B$  has a SHAP value of 0.035. In contrast, the variables roughness and  $\rho B/c_{\rm uo}$  exhibit the least influence, with their SHAP values approaching zero. These results underscore the pivotal role of  $\varphi$ ' in predicting bearing capacity, while emphasizing the limited impact of roughness and  $\rho B/c_{\rm uo}$  on the model's overall performance.

The findings from the Shapley values analysis provide valuable insights with practical implications for decision-making in selecting design parameters. Here are some practical implications of the outcomes:

(1) Internal friction angle  $\varphi$ ': The high SHAP value of  $\varphi$ ' underscores its significant influence on bearing capacity.

**Table 5**Comparison of evaluation metrics for models using 10-fold cross-validation.

Models	Test	Test			Train		
	MSE	MAE	$R^2$	MSE	MAE	R <sup>2</sup>	
LGB	1.149	0.778	0.996	0.573	0.566	0.998	
XGB	0.648	0.498	0.998	0.073	0.187	1.000	
CatB	0.377	0.416	0.999	0.122	0.259	1.000	
ANN	1.316	0.834	0.995	1.219	0.802	0.995	
WOA-DNN	0.189	0.314	1.000	0.122	0.261	1.000	

**Table 4** Model parameter information.

Model	Parameter
LGB	$n_{estimators} = 150$ ; $num_{eaves} = 25$ ; $learning_{rate} = 0.15$ ; $reg_{estimators} = 0.02$ ; $reg_{estimators} = 0.02$
XGB	$learning\_rate = 0.1; n\_estimators = 200; max\_depth = 8; subsample = 1; colsample\_bytree = 1; gamma = 0.01; min\_child\_weight = 1$
CatB	Iterations = $1000$ ; depth = $8$ ;
ANN	number of neuron = 100; activations = 'Relu'; optimization algorithm = 'Adamax '
WOA-DNN	number of neuron $= 100$ ; number of layers $= 4$ ; activations $= $ 'Relu'; optimization algorithm $= $ 'Adamax '; learning rate $= 0.01$

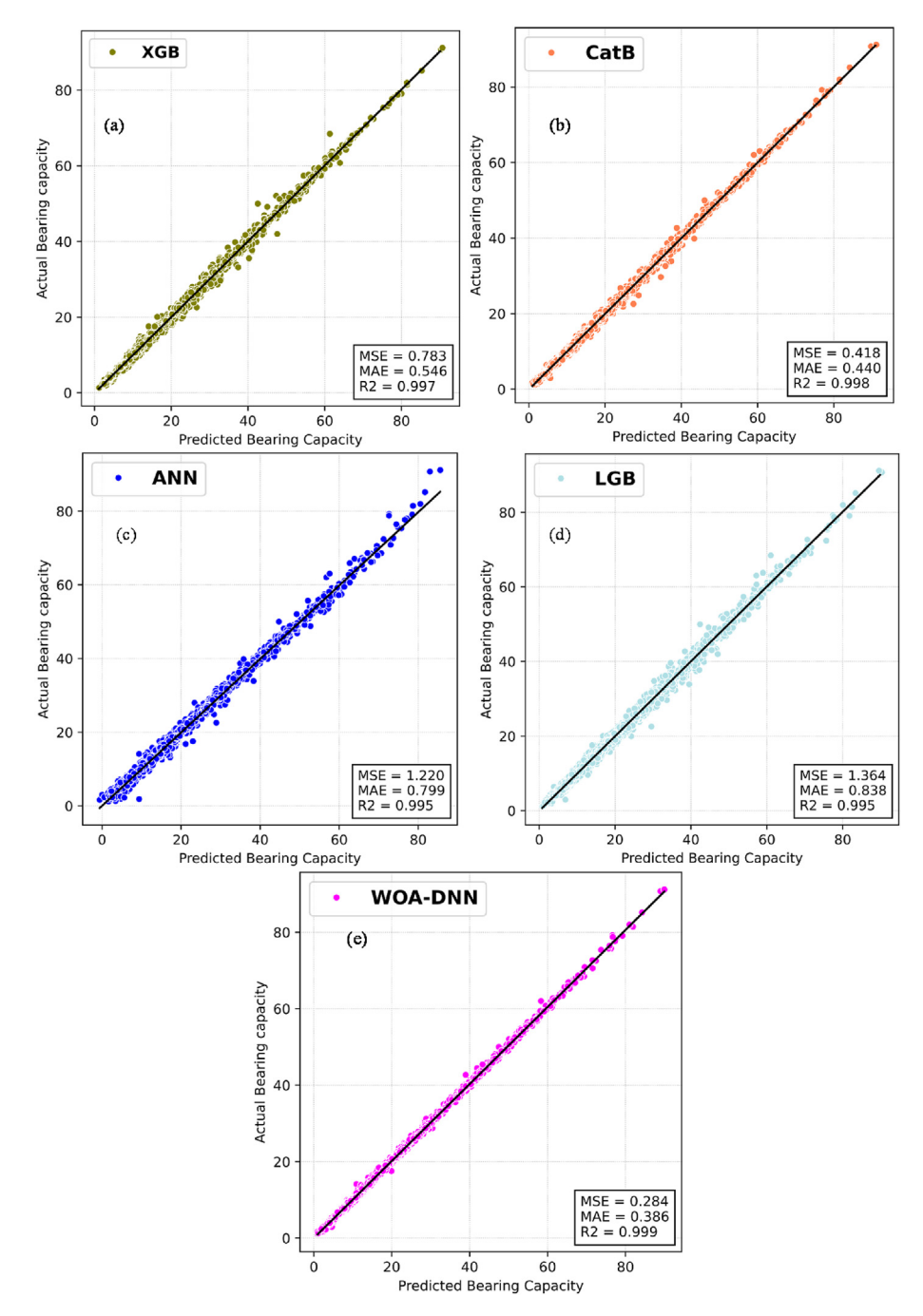


Fig. 22. Comparing the best performance of four models in the regression plot: (a) XGB, (b) CatB, (c) ANN, (d) LGB, and (e) WOA-DNN.

Designers and engineers should pay close attention to the value of the angle of internal friction  $(\varphi')$  when planning strip footing designs. It's essential to select an appropriate  $\varphi'$  value to ensure the stability and load-bearing capacity of the foundation.

- (2) The strength ratio  $c_{\rm uo}/\gamma B$ : The SHAP value of  $c_{\rm uo}/\gamma B$  highlights its substantial contribution to bearing capacity. Designers should carefully evaluate this parameter when assessing the design, as it plays a crucial role in determining the load-bearing capacity of strip footings.
- (3) The depth ratio  $H_1/B$  and the surcharge ratio  $q/\gamma B$ :  $H_1/B$  and  $q/\gamma B$  also have notable impacts on bearing capacity. Engineers should consider these parameters in the design process

- and adjust them according to project requirements and soil conditions.
- (4) Low Priority on Roughness and  $\rho B/c_{uo}$ : The low SHAP values for roughness and  $\rho B/c_{uo}$  indicate their limited influence on bearing capacity. While these parameters should not be ignored, designers may allocate less effort in optimizing or adjusting them, especially when compared to the more critical factors like  $\varphi$ ' and  $c_{uo}/\gamma B$ .

To make informed decisions, engineers may consider conducting thorough soil testing and data collection, particularly for  $\varphi$ ' and  $c_{uo}/\gamma B$ . Accurate and precise measurements and assessments of these parameters will lead to more reliable and stable strip footing

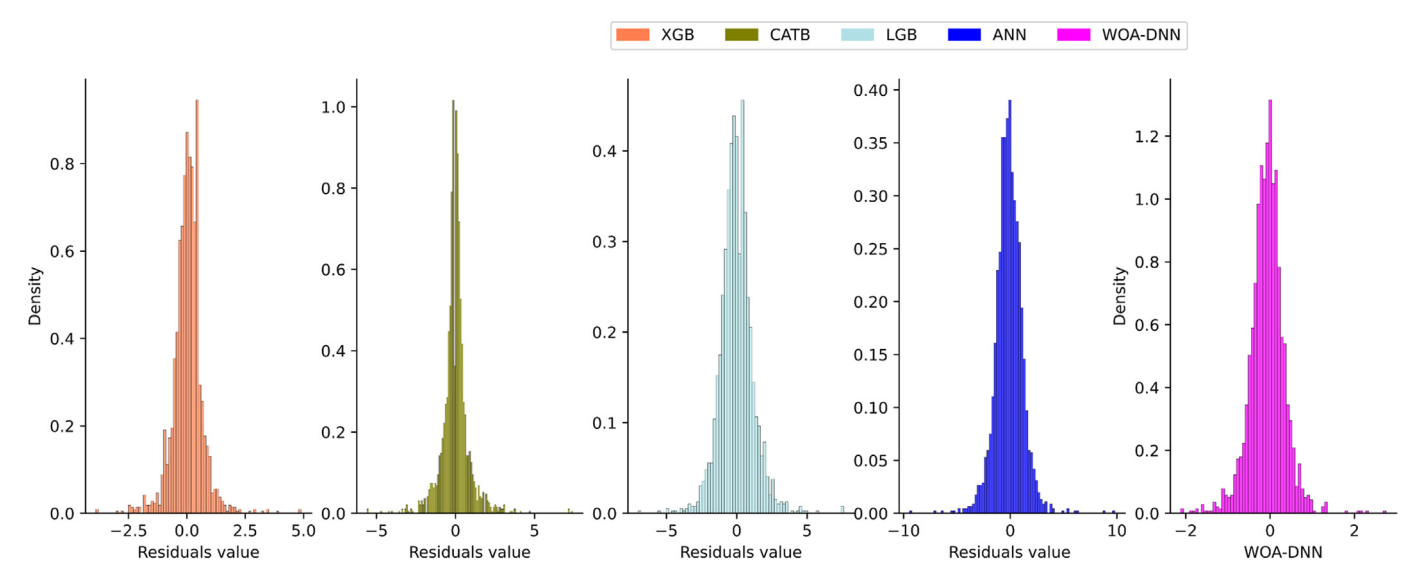


Fig. 23. A comparison of residual value densities for five models in the histogram plot.

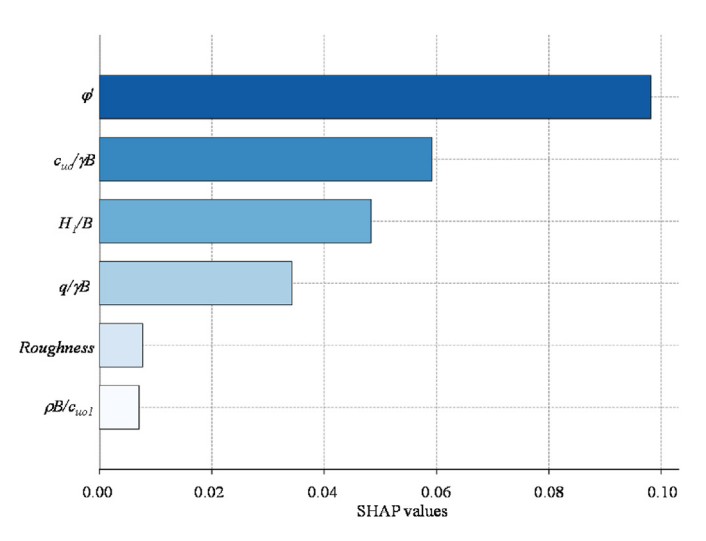


Fig. 24. Shapley values for feature importance.

designs. By understanding the relative importance of each feature, they can focus on improving and refining the design parameters that have the most substantial impact on bearing capacity.

#### 6.2. Partial dependence plots (PDPs)

The Partial Dependence Plots (PDPs) are useful tools that can provide valuable insights into how each input variable impacts the bearing capacity of strip footings on clayey layers (ref. Fig. 25). The PDPs illustrate the relationship between individual input variables and the output variable, i.e. the bearing capacity  $(p/\gamma B)$ . Here's a detailed discussion of the PDPs for each input variable:

(1) *H*<sub>1</sub>/*B*: The PDP for *H*<sub>1</sub>/*B* shows that varying this parameter from 0.25 to 1.75 leads to a substantial increase in bearing capacity, ranging from 15 to 32.5. This indicates that increasing the relative depth of the sand layer compared to the footing width has a significant positive effect on the bearing capacity. Designing a deeper sand layer enhances the load-bearing capacity of the foundation.

- (2)  $q/\gamma B$ : The PDP for  $q/\gamma B$  reveals that varying this parameter from 0 to 1 results in an increase in bearing capacity, ranging from 16 to 26. It suggests that an increase in applied load relative to the soil unit weight and footing width contributes positively to the bearing capacity. This insight can guide designers in optimizing load distribution on footings for improved performance.
- (3)  $\varphi$ ': The PDP for  $\varphi$ ' illustrates that varying this parameter from 20° to 45° leads to a substantial increase in bearing capacity, ranging from 5 to approximately 40. It shows that increasing the internal friction angle of the soil has a highly positive influence on bearing capacity. Selecting soils with a higher internal friction angle can significantly enhance foundation performance.
- (4)  $c_{\rm uo}/\gamma B$ : The PDP for  $c_{\rm uo}/\gamma B$  demonstrates that varying this parameter from 0.2 to 5 results in an increase in bearing capacity, ranging from 10 to 30. It highlights that increasing the cohesion of the soil relative to the soil unit weight and footing width has a strong positive impact on bearing capacity. This insight can guide designers in selecting or improving soil types for better foundation support.
- (5)  $\rho B/c_{uo}$ : The PDP for  $\rho B/c_{uo}$  indicates that an increase in this parameter from 0 to 1 leads to a minor increase in bearing capacity, from 20.5 to 23.5. While the effect is relatively small, it emphasizes that this parameter has a limited effect on the bearing capacity in comparison to other design factors.
- (6) Roughness: The PDP for footing roughness shows that shifting from a smoother to a rougher footing surface results in an increase in bearing capacity, ranging from 21.5 to 23. It highlights the role of surface roughness in enhancing the footing's ability to withstand loads, though not significant like other design factors.

To gain deeper insights into the physical mechanisms influencing load-bearing capacity on layered soils, a comprehensive feature interaction analysis between pairs of variables was conducted. This analysis, illustrated in Figs. 26–36, includes both two-dimensional and three-dimensional visualizations. These visualizations uncover intricate relationships and dependencies among key variables such as footing roughness,  $H_1/B$  ratio,  $q/\gamma B$  ratio, internal friction angle  $(\varphi')$ , cohesion  $(c_{uo}/\gamma B)$ , and  $\rho B/c_{uo}$  ratio.

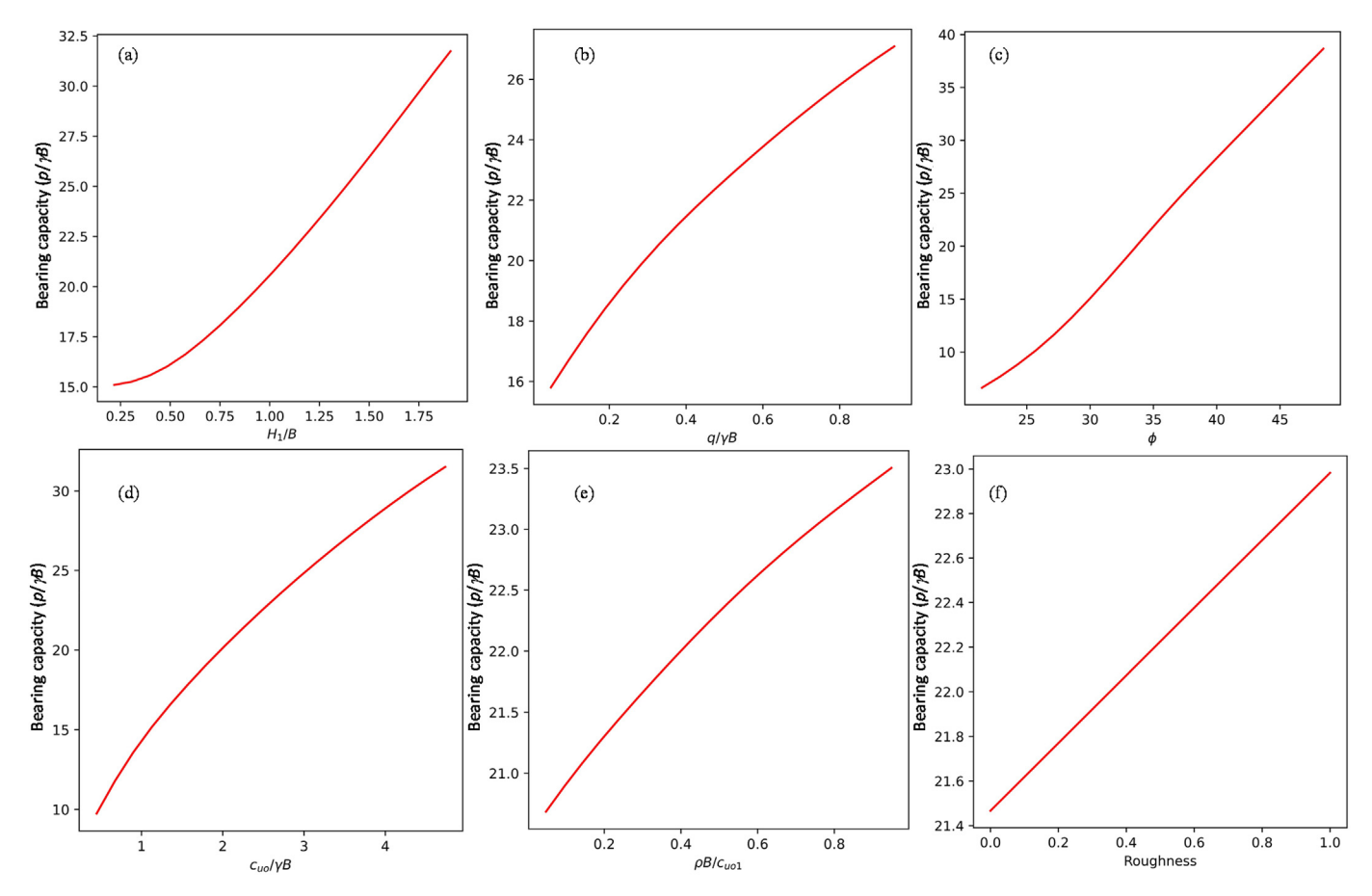


**Fig. 25.** Results of PDPs study: (a)  $H_1/B$ , (b)  $q/\gamma B$ , (c)  $\varphi'$ , (d)  $c_{uo}/\gamma B$ , (e)  $\rho B/c_{uo}$ , and (f) Roughness.

The two-dimensional plots highlight the direct impact of footing roughness on variables like  $H_1/B$  and  $q/\gamma B$ , providing a clear view of how changes in one variable affect the overall load-bearing capacity in conjunction with another. The three-dimensional plots, on the other hand, offer a more comprehensive perspective, illustrating how multiple factors interact simultaneously.

These findings are invaluable for optimizing strip footing design.

The detailed insights from the feature interaction analysis enable engineers to make informed decisions by considering the combined effects of various design parameters. This approach leads to more accurate predictions of bearing capacity and enhances the reliability and safety of foundation designs. The ability to visualize and understand these complex interactions supports the development of more effective and efficient geotechnical engineering solutions,

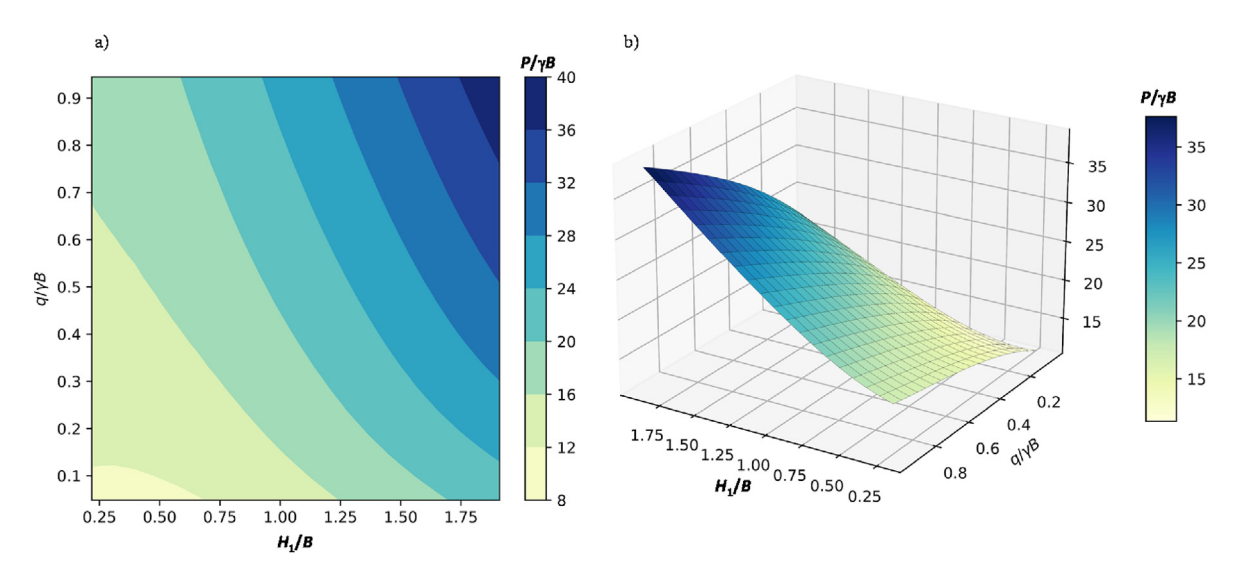


**Fig. 26.** Feature interaction analysis between  $H_1/B$  and  $q/\gamma B$ : (a) 2D visualization and (b) 3D visualization.

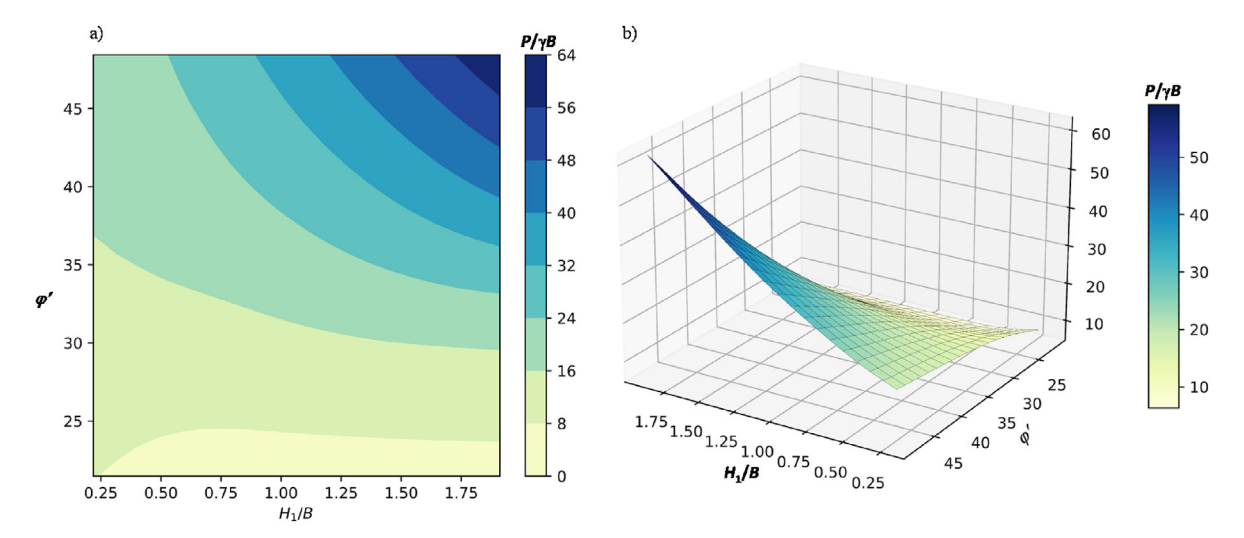


**Fig. 27.** Feature interaction analysis between  $H_1/B$  and  $\varphi'$ : (a) 2D visualization and (b) 3D visualization.

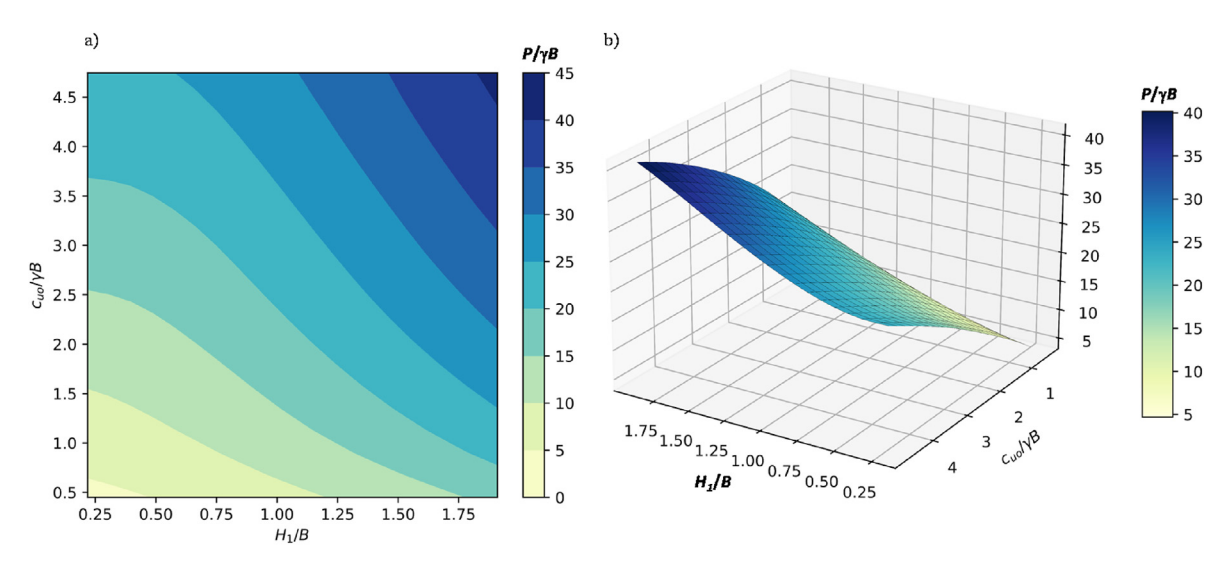


**Fig. 28.** Feature interaction analysis between  $H_1/B$  and  $c_{uo}/\gamma B$ : (a) 2D visualization and (b) 3D visualization.

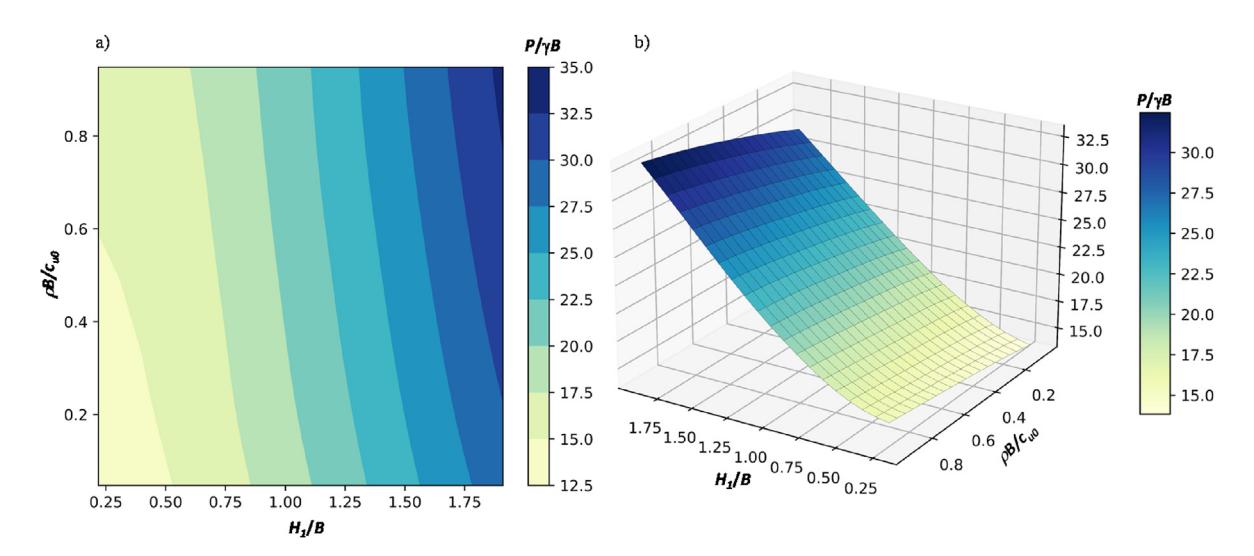


**Fig. 29.** Feature interaction analysis between  $H_1/B$  and  $\rho B/c_{uo}$ : (a) 2D visualization and (b) 3D visualization.

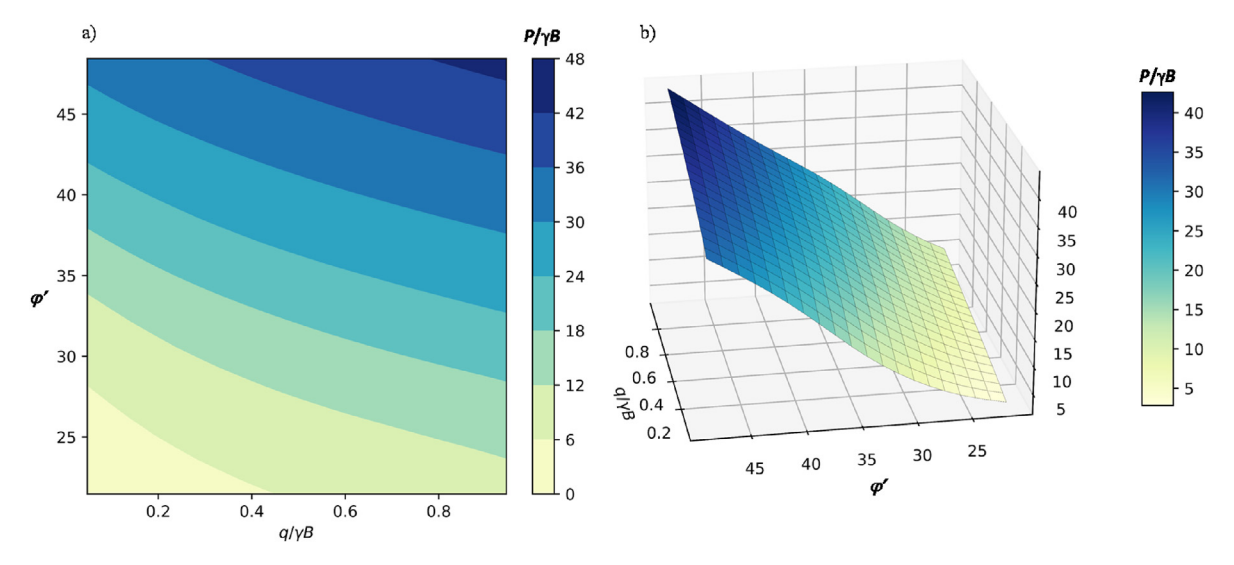


**Fig. 30.** Feature interaction analysis between  $\varphi'$  and  $q/\gamma B$ : (a) 2D visualization and (b) 3D visualization.

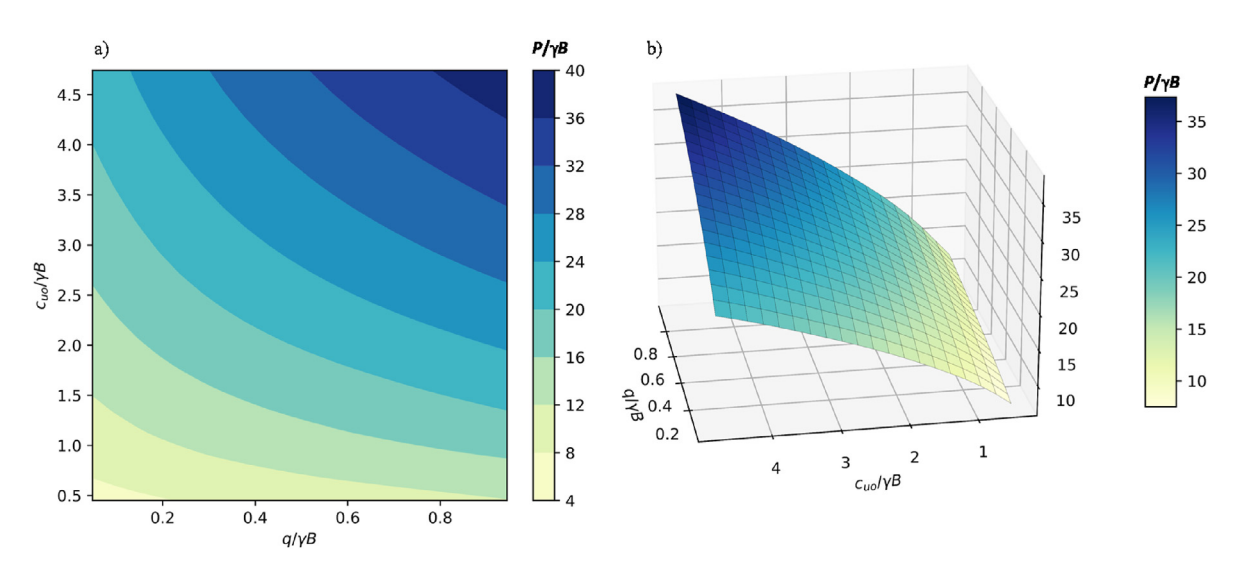


**Fig. 31.** Feature interaction analysis between  $c_{uo}/\gamma B$  and  $q/\gamma B$ : (a) 2D visualization and (b) 3D visualization.

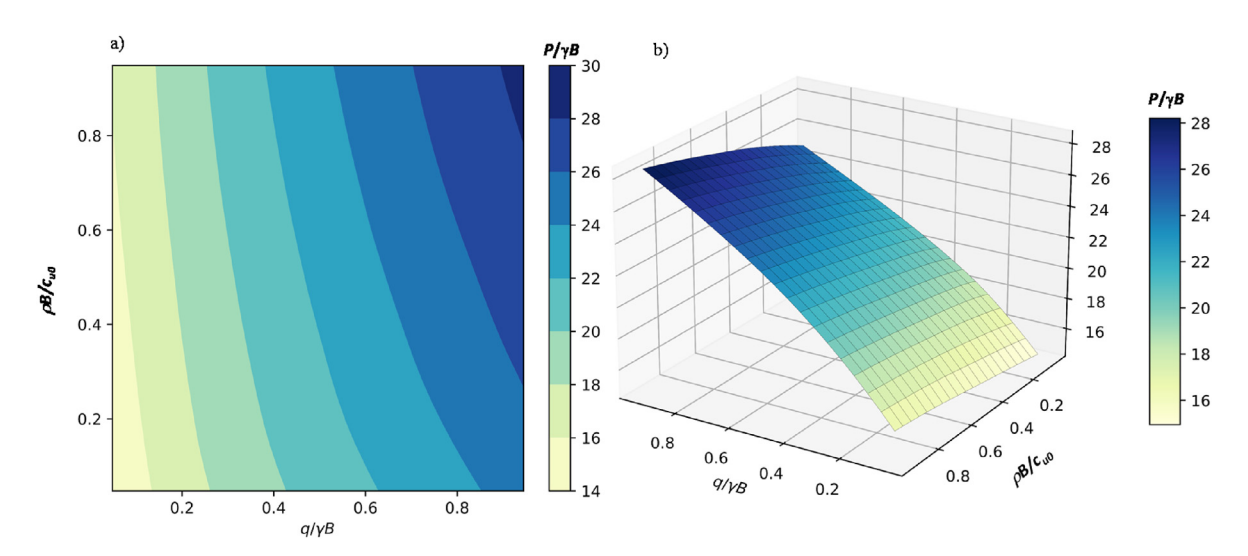


**Fig. 32.** Feature interaction analysis between  $\rho B/c_{uo}$  and  $q/\gamma B$ : (a) 2D visualization and (b) 3D visualization.

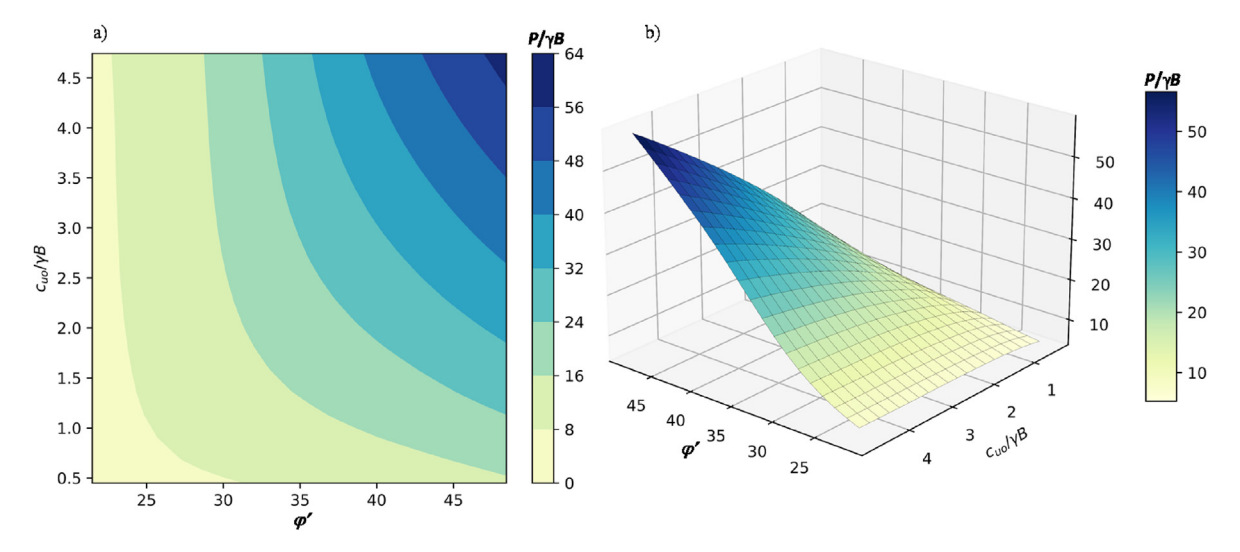


**Fig. 33.** Feature interaction analysis between  $\varphi'$  and  $c_{uo}/\gamma B$ : (a) 2D visualization and (b) 3D visualization.

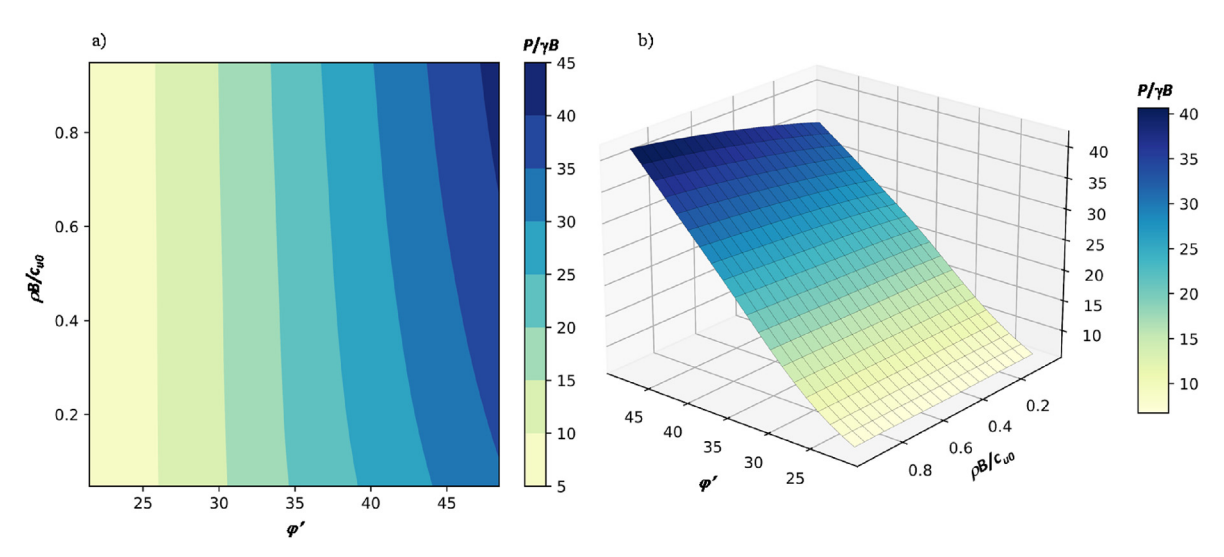


**Fig. 34.** Feature interaction analysis between  $\varphi'$  and  $\rho B/c_{uo}$ : (a) 2D visualization and (b) 3D visualization.

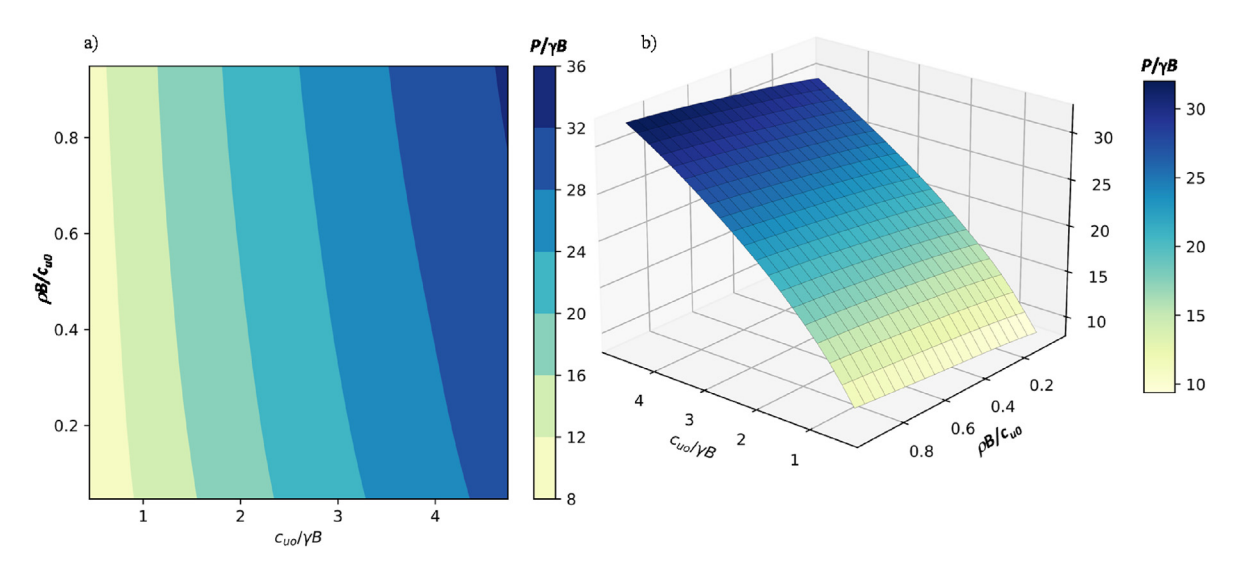


**Fig. 35.** Feature interaction analysis between  $\rho B/c_{uo}$  and  $c_{uo}/\gamma B$ : (a) 2D visualization and (b) 3D visualization.

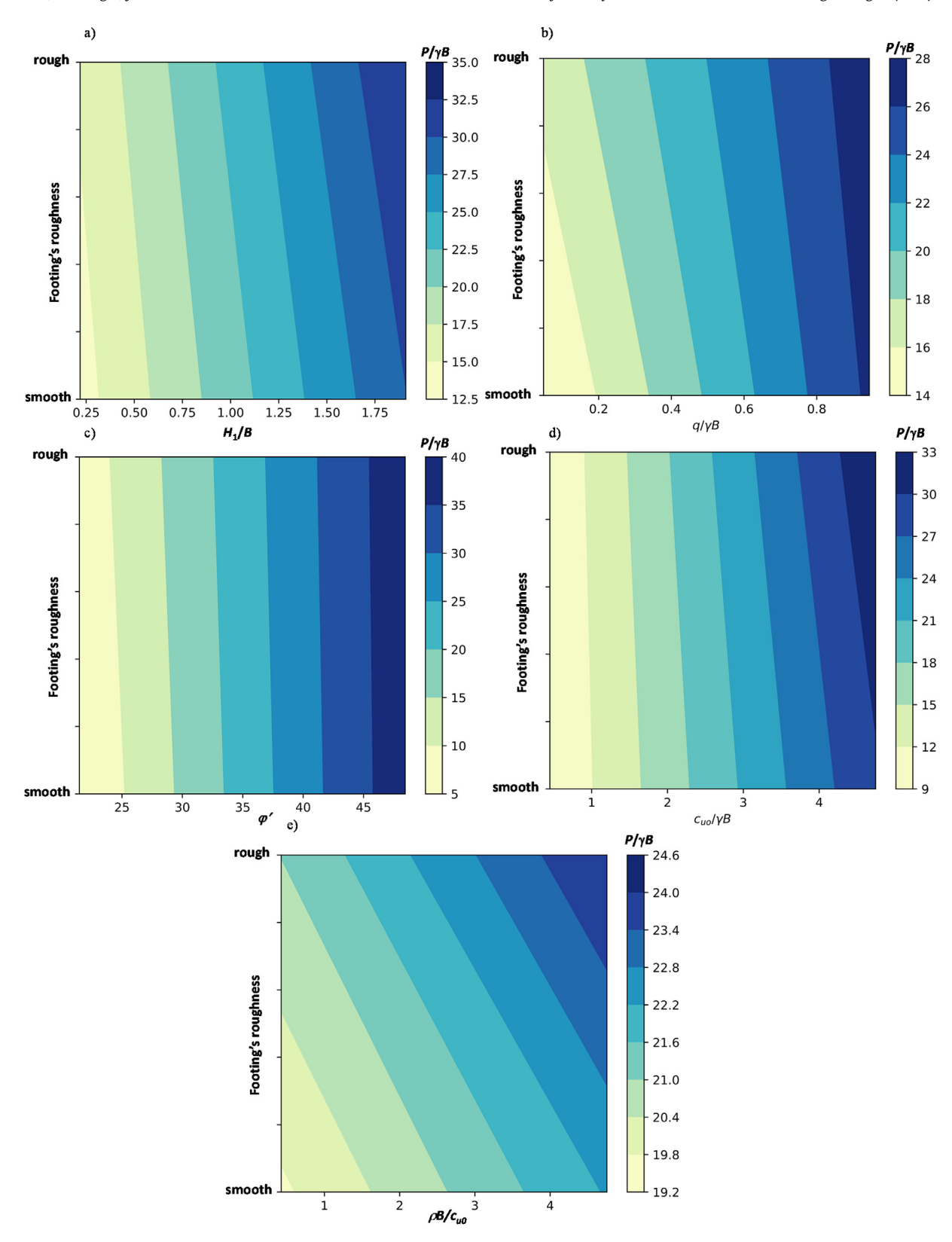


**Fig. 36.** 2D visualization of Feature interaction between footing roghness and: (a)  $H_1/B$ , (b)  $q/\gamma B$ , (c)  $\varphi'$ , (d) $c_{uo}/\gamma B$ , and (e)  $\rho B/c_{uo}$  (Note: Since footing roughness only has two scenarios: smooth or rough; only 2D visualizations are plotted).

ultimately facilitating the optimization of strip footing designs for better performance and safety.

In summary, designers can optimize the bearing capacity of strip footings on clayey layers by manipulating these input parameters. For instance, they may opt for a deeper sand layer  $(H_1/B)$  or select soils with higher internal friction angles  $(\varphi')$  to improve foundation performance. The Partial Dependence Plots (PDPs) provide a quantitative understanding of how these changes impact bearing capacity, leading to better design choices and safer construction practices. This comprehensive analysis empowers engineers to enhance foundation design, ensuring greater structural integrity and stability.

#### 7. Conclusions

This study effectively implemented a data-driven approach using the WOA-DNN, optimized by the WOA, to predict the bearing capacity of sand over clay. By combining IGA with UB limit analysis, this innovative methodology presents a promising solution for achieving more accurate and efficient designs in geotechnical engineering.

The analysis has clearly demonstrated the significant impact of various design parameters on bearing capacity. Specifically, the depth ratio  $(H_1/B)$ , surcharge ratio  $(q/\gamma B)$ , and internal friction angle  $(\varphi')$  have been shown to substantially enhance bearing capacity. Designing with thicker sand layers, higher surcharge ratios, and soils with greater internal friction angles leads to improved foundation performance. Furthermore, the study indicates that an increase in the soil strength ratio  $(c_{uo}/\gamma B)$  leads to a corresponding rise in bearing capacity. Although footing surface roughness plays a lesser role compared to other factors, it still contributes to improved load-bearing capacity. These insights offer designers and engineers a thorough understanding of how to optimize bearing capacity in geotechnical applications. By focusing on key parameters such as  $H_1/B$ ,  $q/\gamma B$ ,  $\varphi'$ , and  $c_{uo}/\gamma B$ , design decisions can be made with greater precision, leading to safer and more efficient construction practices. This quantitative analysis of parameter impacts aids in developing more effective geotechnical solutions.

The study also showcased the effectiveness of the WOA-DNN model, inspired by the bubble-net hunting strategy of humpback whales, in tackling complex optimization problems in geotechnical engineering. Through extensive experimentation and validation, the research demonstrated the model's superior performance in addressing challenging scenarios that conventional methods often fail to consider effectively. By incorporating advanced techniques like feature importance analysis and partial dependence plots, the study offered strong evidence of the model's capacity to uncover key insights into the factors influencing bearing capacity determination. The integration of advanced numerical methods with ML not only improves current practices but also establishes a foundation for future innovations, aimed at promoting better design outcomes and contributing to advancing the field of geotechnical engineering.

#### 8. Limitations and future works

This study primarily focuses on static conditions for strip footings on layered soils, representing an initial step in exploring datadriven methodologies for bearing capacity analysis. Future research should aim to broaden and refine these methodologies in several key areas. Firstly, extending the analysis to incorporate dynamic conditions, such as seismic loading, will be crucial to understanding the full spectrum of foundation behavior in varying environmental contexts. Additionally, there is a need to consider more complex practical scenarios, including adjacent footings, sloped footings,

and footings over voids, under both static and dynamic conditions.

Moreover, further development of the proposed data-driven approach could benefit from incorporating larger and more diverse datasets. This expansion would improve model robustness and enhance its ability to generalize across a wider range of soil types and structural configurations. Exploring advanced ML techniques, such as deep reinforcement learning or ensemble methods, could also contribute to refining predictive accuracy and resilience in challenging geotechnical scenarios.

Ultimate goals include the development of user-friendly software tools that integrate these advanced methodologies, making them accessible for practical engineering applications. By addressing these future directions, subsequent studies can build on the foundation established by this research, advancing the field of geotechnical stability designs to more accurate, reliable, and versatile solutions.

#### **CRediT authorship contribution statement**

**Toan Nguyen-Minh:** Writing — original draft, Visualization, Validation, Software, Methodology, Investigation, Formal analysis, Data curation. **Tram Bui-Ngoc:** Visualization, Software, Methodology, Investigation, Formal analysis, Data curation. **Jim Shiau:** Writing — review & editing, Validation. **Tan Nguyen:** Writing — review & editing, Writing — original draft, Validation, Supervision, Project administration, Investigation, Conceptualization. **Trung Nguyen-Thoi:** Writing — review & editing.

## Data availability

The data used in the current study are available from the corresponding author upon reasonable request.

#### **Declaration of competing interest**

The authors declare that they have no known competing financial interests or personal relationships that could have appeared to influence the work reported in this paper.

# Acknowledgements

The first author expresses gratitude for the insightful guidance provided by Assoc. Prof. Tuan-Anh Tran at Ho Chi Minh City University of Technology (HCMUT) during their master's course from 2012 to 2014. Special appreciation is extended to Dr. Chanh-Hoang Nguyen (Imperial College London, UK) for his expert contribution in integrating Smooth FEM into Limit Analysis, a pivotal element in the evolution of the IGA-UB framework in 2012—2013. Finally, we are deeply appreciative of the invaluable feedback provided by the anonymous reviewers.

#### References

Burd, H.J., Frydman, S., 1997. Bearing capacity of plane-strain footings on layered soils. Can. Geotech. J. 34 (2), 241–253.

Craig, W.H., Chua, K., 1990. Deep penetration of spud-can foundations on sand and clay. Geotechnique 40 (4), 541–556.

Chen, T., Guestrin, C., 2016. XGBoost: a scalable tree boosting system. In: 22nd Acm Sigkdd International Conference on Knowledge Discovery and Data Mining, pp. 785–794.

Cheng, Z.L., Kannangara, K.K.P.M., Su, L.J., Zhou, W.H., 2023a. Mathematical model for approximating shield tunneling-induced surface settlement via multi-gene genetic programming. Acta Geotech 18 (9), 4923–4940.

Cheng, Z.L., Kannangara, K.K.P.M., Su, L.J., Zhou, W.H., Tian, C., 2023b. Physics-guided genetic programming for predicting field-monitored suction variation with effects of vegetation and atmosphere. Eng. Geol. 315, 107031.

Cheng, Z., Zhou, W., Tian, C., 2022. Multi-perspective analysis on rainfall-induced spatial response of soil suction in a vegetated soil. J. Rock Mech. Geotech.

- Eng. 14 (4), 1280-1291.
- Ebid, A.M., Onyelowe, K.C., Salah, M., Castaldo, P., 2022. Estimation of bearing capacity of strip footing rested on bilayered soil profile using FEM-Al-coupled techniques. Adv. Civ. Eng. 2022, 1-11.
- Goodfellow, I., Bengio, Y., Courville, A., 2016. Deep Learning. MIT Press.
- Griffiths, D.V., 1982. Computation of bearing capacity factors using finite elements. Geotechnique 32 (3), 195-202.
- Haghighi, A., Hu, P., Tom, J.G., Krabbenhoft, K., 2019. Combined loading of strip footings on sand-over-clay with layers of varying extents. Soils Found. 59 (2), 433-442.
- Hanna, A.M., 1981, Experimental study on footings in layered soil, I. Geotech, Eng. Div. 107 (8), 1113-1127.
- Hanna, A.M., 1982. Bearing capacity of foundations on a weak sand layer overlying a strong deposit. Can. Geotech. J. 19 (3), 392-396.
- Hanna, A.M., Meyerhof, G.G., 1980. Design charts for ultimate bearing capacity of foundations on sand overlying soft clay. Can. Geotech. J. 17 (2), 300–303.
- Huang, M., Qin, H.L., 2009. Upper-bound multi-rigid-block solutions for bearing capacity of two-layered soils. Comput. Geotech. 36 (3), 525–529.
- Hughes, T.J.R., Cottrell, J.A., Bazilevs, Y., 2005. Isogeometric analysis: CAD, finite elements, NURBS, exact geometry and mesh refinement. Comput. Methods Appl. Mech. Eng. 194 (39–41), 4135–4195.
- Ke, G., Meng, Q., Finley, T., Wang, T., Chen, W., Ma, W., Ye, Q., Liu, T.Y., 2017. Lightgbm: a highly efficient gradient boosting decision tree. In: Proceedings of the 31st International Conference on Neural Information Processing Systems, pp. 3149-3157
- Lee, K.K., Randolph, M.F., Cassidy, M.J., 2013a. Bearing capacity on sand overlying clay soils: a simplified conceptual model. Geotechnique 63 (15), 1285–1297.
- Lee, K.K., Cassidy, M.J., Randolph, M.F., 2013b. Bearing capacity on sand overlying clay soils: experimental and finite-element investigation of potential punchthrough failure. Geotechnique 63 (15), 1271-1284.
- Ly, D.K., Vu, H.N., Thongchom, C., Nguyen-Thoi, T., 2024. A multi-physical coupling isogeometric formulation for nonlinear analysis and smart control of laminated CNT-MEE plates. Eng. Anal. Bound. Elem. 159, 36-57.
- Makrodimopoulos, A., Martin, C.M., 2007. Upper bound limit analysis using simplex strain elements and second-order cone programming. Int. J. Numer. Anal. Methods GeoMech. 31 (6), 835-865.
- Meyerhof, G.G., 1974. Ultimate bearing capacity of footings on sand layer overlying clay. Can. Geotech. J. 11 (2), 223-229.
- Michalowski, R.L., Shi, L., 1995. Bearing capacity of footings over two-layer foundation soils. J. Geotech. Eng. 121 (5), 421-428.
- Mirjalili, S., Lewis, A., 2016. The whale optimization algorithm. Adv. Eng. Software 95. 51-67.
- Moayedi, H., Rezaei, A., 2020. The feasibility of PSO-ANFIS in estimating bearing capacity of strip foundations rested on cohesionless slope. Neural Comput. Appl. 33 (9), 4165-4177.
- Moayedi, H., Nguyen, H., Rashid, A.S.A., 2019a. Novel metaheuristic classification approach in developing mathematical model-based solutions predicting failure in shallow footing. Eng. Comput. 37 (1), 223-230.
- Moayedi, H., Abdullahi, M.a.M., Nguyen, H., Rashid, A.S.A., 2019b. Comparison of dragonfly algorithm and Harris hawks optimization evolutionary data mining techniques for the assessment of bearing capacity of footings over two-layer foundation soils. Eng. Comput. 37 (1), 437-447.
- Najafabadi, M.M., Villanustre, F., Khoshgoftaar, T.M., Seliya, N., Wald, R., Muharemagic, E., 2015. Deep learning applications and challenges in big data analytics. J. Big Data 2, 1.
- Nikbakht, M., Sarand, F.B., Esmatkhah Irani, A., Hajialilue Bonab, M., Azarafza, M., Derakhshani, R., 2022. An experimental study for swelling effect on repairing of cracks in fine-grained clayey soils. Appl. Sci. 12 (17), 8596.
- Nguyen-Minh, T., Bui-Ngoc, T., Shiau, J., Nguyen, T., Nguyen-Thoi, T., 2023. Coupling isogeometric analysis with deep learning for stability evaluation of rectangular tunnels. Tunn. Undergr. Space Technol. 140, 105330.
- Nguyen-Minh, T., Bui-Ngoc, T., Shiau, J., Nguyen, T., Nguyen-Thoi, T., 2024. Undrained sinkhole stability of circular cavity: a comprehensive approach based on isogeometric analysis coupled with machine learning. Acta Geotech. https:// doi.org/10.1007/s11440-024-02266-3.
- Nguyen-Thoi, T., Ly, D.K., Kattimani, S., Thongchom, C., 2023. An electromechanical coupling isogeometric approach using zig-zag function for modeling and smart

- damping control of multilayer PFG-GPRC plates. Acta Mech. 235, 941-970.
- Nguyen, T.H., Nguyen, T., Truong, T.T., Doan, D.T.V., Tran, D.H., 2023. Corrosion effect on bond behavior between rebar and concrete using Bayesian regularized feedforward neural network. Structures 51, 1525-1538.
- Nguyen, T., Tran, L.V., 2021. Arching effect in sand piles under base deflection using geometrically non-linear isogeometric analysis. Geomech. Eng. 26 (4). 369-384.
- Nguyen, T., Ly, D.K., Shiau, J., Nguyen-Dinh, P., 2024. Optimizing load-displacement prediction for bored piles with the 3mSOS algorithm and neural networks. Ocean. Eng. 304, 117758.
- Nguyen, T., Truong, T.T., Nguyen-Thoi, T., Van Hong Bui, L., Nguyen, T.H., 2022. Evaluation of residual flexural strength of corroded reinforced concrete beams using convolutional long short-term memory neural networks. Structures 46, 899-912
- Okamura, M., Takemura, J., Kimura, T., 1997. Centrifuge model tests on bearing capacity and deformation of sand layer overlying clay. Soils Found. 37 (1), 73–88.
- Okamura, M., Takemura, J., Kimura, T., 1998. Bearing capacity predictions of sand overlying clay based on limit equilibrium methods. Soils Found, 38 (1), 181-194
- Prokhorenkova, L., Gusev, G., Vorobev, A., Dorogush, A.V., Gulin, A., 2018, CatBoost: unbiased boosting with categorical features. In: Proceedings of the 32nd International Conference on Neural Information Processing Systems. pp. 6639-6649.
- Pham, Q.N., Ohtsuka, S., 2021. Ultimate bearing capacity of rigid footing on twolayered soils of sand—clay. Int. J. GeoMech. 21 (7), 0002095. Rajaei, A., Keshavarz, A., Ghahramani, A., 2018. Static and seismic bearing capacity
- of strip footings on sand overlying clay soils. Iran. J. Sci. Technol.-Trans. Civ. Eng. 43 (1), 69-80.
- Salimi Eshkevari, S., Abbo, A.J., Kouretzis, G., 2019. Bearing capacity of strip footings
- on sand over clay. Can. Geotech. J. 56 (5), 699–709. Shiau, J.S., Lyamin, A.V., Sloan, S.W., 2003. Bearing capacity of a sand layer on clay by finite element limit analysis. Can. Geotech. J. 40 (5), 900-915.
- Shoaei, M.D., Alkarni, A., Noorzaei, J., Jaafar, M.S., Huat, B.B.K., 2012. Review of available approaches for ultimate bearing capacity of two-layered soils. J. Civ. Eng. Manag. 18 (4), 469-482.
- Tang, C., Phoon, K.-K., Zhang, L., Li, D.Q., 2017. Model uncertainty for predicting the bearing capacity of sand overlying clay. Int. J. GeoMech. 17 (7), 0000898.
- Teh, K.L., Leung, C.F., J, Y.K.C.M., 2010. Centrifuge model study of spudcan penetration in sand overlying clay. Geotechnique 60 (11), 825-842.
- Teh, K.L., Cassidy, M.J., Leung, C.F., Chow, Y.K., Randolph, M.F., Quah, C.K., 2008. Revealing the bearing capacity mechanisms of a penetrating spudcan through sand overlying clay. Geotechnique 58 (10), 793-804.
- Van Tran, M., Ly, D.-K., Nguyen, T., Tran, N., 2024. Robust prediction of workability properties for 3D printing with steel slag aggregate using bayesian regularization and evolution algorithm. Construct. Build. Mater. 431, 136470.
- Wani, M.A., Bhat, F.A., Afzal, S., Khan, A.I., 2020. Advances in Deep Learning. Springer.
- Wong, P.C., Templeton III, J., Purwana, O.A., Hugo, H., Cassidy, M.J., Hossain, M.S. Martin, C., 2012. Foundation modeling and assessment in the new ISO standard 19905-1. In: Offshore Technology Conference. OTC. OTC-23521-MS.



Dr. Nguyen Tan received his PhD from Kyoto University, Japan, specializing in geotechnical engineering. His research encompasses computational geomechanics, soil plasticity, numerical methods, and smart computing in civil engineering. As head of the Smart Computing in Civil Engineering Research Group (SCCE) at Ton Duc Thang University (TDTU), Dr. Tan focuses on coupling robust computational methods with smart computing to address a wide range of problems in civil engineering, with a commitment to bridging theory and practical applications in infrastructure development.